Intra-unit-cell Nematic Density Wave: Unified Broken-Symmetry of the Cuprate Pseudogap State

K. Fujita[a,b,c,†], M. H. Hamidian[a,b,†], S.D. Edkins[b,d], Chung Koo Kim[a], Y. Kohsaka[e], M. Azuma[f], M. Takano[g], H. Takagi[c,h,i], H. Eisaki[j], S. Uchida[c], A. Allais[k], M. J. Lawler[b,l], E. -A. Kim[b], S. Sachdev[k] & J. C. Séamus Davis[a,b,d]

a. *CMPMS Department, Brookhaven National Laboratory, Upton, NY 11973, USA.*
b. *LASSP, Department of Physics, Cornell University, Ithaca, NY 14853, USA.*
c. *Department of Physics, University of Tokyo, Bunkyo-ku, Tokyo 113-0033, Japan.*
d. *School of Physics and Astronomy, University of St. Andrews, Fife KY16 9SS, Scotland.*
e. *RIKEN Center for Emergent Matter Science, Wako, Saitama 351-0198, Japan.*
f. *Materials and Structures Lab., Tokyo Institute of Technology, Yokohama, Kanagawa 226-8503, Japan*
g. *Institute for Integrated Cell-Material Sciences, Kyoto University, Sakyo-ku, Kyoto 606-8501, Japan*
h. *RIKEN Advanced Science Institute, Wako, Saitama 351-0198, Japan.*
i. *Max-Planck-Institut für Festkörperforschung, Heisenbergstraße 1 70569 Stuttgart, Germany*
j. *Institute of Advanced Industrial Science and Technology, Tsukuba, Ibaraki 305-8568, Japan.*
k. *Department of Physics, Harvard University, Cambridge, MA.*
l. *Dept. of Physics and Astronomy, Binghamton University, Binghamton, NY 13902.*

† *These authors contributed equally to this project.*

The identity of the fundamental broken symmetry (if any) in the cuprate pseudogap state is unresolved. In fact, two apparently distinct forms of electronic symmetry breaking, one of intra-unit-cell rotational symmetry (Q=0 nematic) and the other of lattice translational symmetry (Q≠0 density wave), are reported extensively. However, indications of linkage between these two phenomena suggest the prospect of a unified fundamental description, with one intriguing possibility being an intra-unit-cell nematic density wave. Here we carry out site-specific measurements within each CuO_2 unit-cell, segregating the results into three separate electronic structure images containing only the Cu sites ($C_u(r)$) and only the x/y-axis O sites ($O_x(r)$ and $O_y(r)$). Phase resolved Fourier analysis reveals directly that the incommensurate modulations in the $O_x(r)$ and $O_y(r)$ sublattice images consistently exhibit a relative phase of π. We confirm this discovery on two highly distinct cuprate compounds, ruling out tunnel matrix-element and materials specific systematics. These observations demonstrate by direct sublattice phase-resolved visualization that the cuprate density wave consists essentially of spatial modulations of the intra-unit-cell nematicity; this state can equally well be described as an intra-unit-cell density wave with a *d*-symmetry form factor.

CuO_2 pseudogap / broken symmetry / intra-unit-cell nematic / density-wave form factor

Electronic Inequivalence at the Oxygen Sites of the CuO_2 Plane in Pseudogap State

Understanding the microscopic electronic structure of the CuO_2 plane represents the essential challenge of cuprate studies. As the density of doped-holes, p, increases from zero in this plane, the pseudogap state (1,2) first emerges, followed by the high temperature superconductivity. Within the elementary CuO_2 unit cell, the Cu atom resides at the symmetry point with an O atom adjacent in the x-axis and y-axis (Fig. 1A). Intra-unit-cell (IUC) degrees of freedom associated with these two O sites (3,4), although often disregarded, may actually represent the key to understanding CuO_2 electronic structure. Among the proposals in this regard are valence-bond ordered phases having spin-singlet occupation only on O_x or O_y sites (5,6), electronic nematic phases having a distinct spectrum of eigenstates at O_x and O_y sites (7,8), and orbital-current phases in which orbitals at O_x and O_y are distinguishable due to time-reversal symmetry breaking (9). A common element to these proposals is that, in the pseudogap state of lightly hole-doped cuprates, some form of electronic symmetry breaking renders the O_x and O_y sites of each CuO_2 unit-cell electronically inequivalent.

Electronic structure studies that discriminate the O_x from O_y sites find a rich phenomenology. Direct oxygen site-specific visualization of electronic structure reveals that even the lightest hole-doping of the insulator immediately produces local IUC symmetry breaking rendering O_x and O_y inequivalent (10); that both $\boldsymbol{Q}\neq 0$ density wave (11) and $\boldsymbol{Q}=0$ IUC nematic state (12) involve electronic inequivalence of the O_x and O_y sites; and that the $\boldsymbol{Q}\neq 0$ and $\boldsymbol{Q}=0$ broken symmetries weaken simultaneously with increasing p and disappear near $p_c=0.19$ (13). For multiple cuprate compounds, neutron scattering reveals clear intra-unit-cell breaking of rotational symmetry (14,15,16). Polar-Kerr effect (17) and thermal transport studies (18) can be likewise interpreted. Similarly, X-ray scattering studies reveal directly the electronic inequivalence between O_x and O_y sites (19), and that scattering at O_x and O_y sites is best modeled by spatially modulating their inequivalence with a d-symmetry form factor (20). Thus, evidence

from a variety of techniques indicates that IUC electronic inequivalence of O_x and O_y is a key element of underdoped-cuprate electronic structure. The apparently distinct phenomenology of $\boldsymbol{Q}\neq 0$ incommensurate density waves (DW) in underdoped cuprates has also been reported extensively (21-28). Moreover, recent studies (29,30) have demonstrated beautifully that the density modulations first visualized by STM imaging (31) are indeed the same as the DW detected by these X-ray scattering techniques. However, although distinct in terms of which symmetry is broken, there is evidence that the $\boldsymbol{Q}=0$ and $\boldsymbol{Q}\neq 0$ states are actually linked microscopically (13,16,20,43,45), thus motivating the search for a unified understanding.

Density Waves that Modulate the CuO_2 Intra-unit-cell States

Logically, such unification might be achieved if there exists some form of density wave that modulates the IUC nematic state. Proposals for such exotic DW states in underdoped cuprates include charge density waves with a *d*-symmetry form factor (32,33) and modulated IUC electron-lattice coupling with a *d*-symmetry form factor (34,35). Modulations of an IUC nematic with wavevectors $\boldsymbol{Q}$=(Q,Q);(Q,-Q) were then explored theoretically (36,37,38,39,40). Most recently, however, focus has sharpened on the models (34,35,40,41,42) yielding spatial modulations of an IUC nematic state that occur at incommensurate wavevectors $\boldsymbol{Q}$=(Q,0);(0,Q) aligned with the CuO_2 plane axes. The microscopics of such models are compared in full detail in SI Section I.

Intra-unit-cell density wave states in the CuO_2 plane (Fig. 1A) can be challenging to conceptualize. Therefore, before explaining their modulated versions, we first describe the elementary symmetry decomposition of the IUC states. Figure 1B,C,D shows the three possible IUC states of CuO_2: a uniform density on the copper atoms (*s*-symmetry), a uniform density on the oxygen atoms (also an *s*-symmetry referred to here as extended-*s* or *s*'-symmetry) and a pattern with opposite-sign density on O_x and

O_y (*d*-symmetry). As they are spatially uniform, these three density patterns correspond to specific representations of the point group symmetry of the lattice. Phase-resolved Fourier transforms of each IUC state (Fig. 1E,F,G) reveal their point group symmetry from the structure of their Bragg peaks. (For simplicity we place the origin at a Cu site and show the real (*Re*) or cosine-component here while the imaginary (*Im*) sine-component is then zero). The *s*-symmetry cases both share 90°-rotational symmetry in their Bragg peak values, while the *d*-symmetry Bragg peaks change sign under 90° rotations. There is also a clear distinction between the two *s*-symmetry patterns: the *s*-form factor has the same magnitude and sign for all Bragg peaks while the *s*'-form factor has a finite peak at (0,0) but vanishing Bragg peaks at (1,0) and (0,1). Thus, by studying the magnitude and sign of the Bragg peak amplitudes in phase-resolved site specific electronic structure images, one can extract the degree to which any IUC pattern has an *s*-, or *s*'- or, as in our previous work (12,13,43,44,45) a *d*-form factor, and their associated symmetries (SI Section II).

Next we consider how a simple periodic modulation of each of these three IUC density patterns with wave vector $\boldsymbol{Q} = (0.25,0) \equiv (Q,0)$, yields three distinct IUC DWs that preserve their respective *s*-, *s*'- and *d*-form factors. Since $\boldsymbol{Q}$ is a vector, however, its directionality breaks rotational symmetry and the resulting DWs are not symmetry distinct. Nevertheless, they are mathematically distinct so that, in principle, one can decompose any CuO_2 IUC DW in terms of its *s*-, *s*'- and *d*-form factor components (SI Section II). To see this, consider the modulated *s*-, *s*'- and *d*-form factor patterns shown in Fig. 2A,B,C. They are constructed by multiplying the corresponding IUC pattern in Fig. 1B,C,D by $\cos(\boldsymbol{Q}\cdot\boldsymbol{r_i})$ where $\boldsymbol{r}_i$ is the location of the i^{th} Cu or O atom with the origin at a Cu site. This yields in Fig. 2A,B,C the $S_{DW}(\boldsymbol{r}) = S\cos(\boldsymbol{Q}\cdot\boldsymbol{r_i})$ for which only Cu sites are relevant, and both $S'_{DW}(\boldsymbol{r}) = S'\cos(\boldsymbol{Q}\cdot\boldsymbol{r_i})$ and $D_{DW}(\boldsymbol{r}) = D\cos(\boldsymbol{Q}\cdot\boldsymbol{r_i})$ for which only the O_x and O_y sites are relevant. Then, the real component of the Fourier

transforms of these patterns, $Re\tilde{S}_{DW}(\boldsymbol{q})$, $Re\widetilde{S'}_{DW}(\boldsymbol{q})$ and $Re\widetilde{D}_{DW}(\boldsymbol{q})$ (Figs. 2D,E,F respectively) preserve the *s*-, *s*'- and *d*-form factors of the IUC density patterns of Figs 1E,F,G respectively. Notice that the *s*-form factor IUC DW has the same sign (Fig. 2D), while the *d*-form factor IUC DW (Fig. 2F) has opposite sign, for the features surrounding the distinct Bragg peaks at $\boldsymbol{Q'} = (1,0)\pm\boldsymbol{Q}$ and $\boldsymbol{Q''}=(0,1)\pm\boldsymbol{Q}$ (compare Fig. 1E,G). However, the most striking contrast between *s*'- and *d*-form factor IUC DW's is manifest by the presence (Fig. 2E) or absence (Fig. 2F) of a peak at the basic modulation wavevector $\boldsymbol{Q}$ within the first Brillouin zone (BZ) (SI Section III). This distinguishing characteristic occurs because the relative phase of π between density on the O_x and O_y sites in the IUC-DW with *d*-form factor results in cancelation of the modulation peak at $\boldsymbol{Q}$ inside the first BZ (SI Section III).

Sublattice-Phase-Resolved Fourier Transform STM

With the recent development of STM techniques to measure IUC electronic structure (10,11,12,13,45) while simultaneously achieving high-precision phase-resolved Fourier analysis (12,13,43,45), it was suggested by one of us (S.S.) that a practical approach to the above challenge would be to separate each such an image of the CuO_2 electronic structure, into three. The first contains only the Cu sites (Cu($\boldsymbol{r}$)) and the other two only the x/y-axis O sites $O_x(\boldsymbol{r})$ and $O_y(\boldsymbol{r})$. The latter are key because the $\widetilde{S'}_{DW}(\boldsymbol{q})$ and $\widetilde{D}_{DW}(\boldsymbol{q})$ are actually formed by using only phenomena from the O_x/O_y sites (Fig. 2B,C). Once the original electronic structure image is thus separated, the phase-resolved Fourier transform of $O_x(\boldsymbol{r})$ and $O_y(\boldsymbol{r})$, $\tilde{O}_x(\boldsymbol{q})$ and $\tilde{O}_y(\boldsymbol{q})$, may, in principle, be used to reveal the form factor of any IUC DW. Thus, an intra-unit-cell nematic DW (IUCN-DW) of *d*-form factor with modulations along both x- and y-axes at $\boldsymbol{Q}=(Q,0);(0,Q)$ should exhibit two key characteristics exemplified by $Re\widetilde{D}_{DW}(\boldsymbol{q})$ shown in Fig. 2I, and whose equivalent experimental information is contained in $Re\tilde{O}_x(\boldsymbol{q}) + Re\tilde{O}_y(\boldsymbol{q})$ (SI Section III). The first is that the modulation peaks at $\boldsymbol{Q}$ should disappear in $Re\tilde{O}_x(\boldsymbol{q}) +$

$Re\tilde{O}_y(\boldsymbol{q})$ while the Bragg-satellite peaks at $\boldsymbol{Q'}$ = (1,0)±$\boldsymbol{Q}$ and $\boldsymbol{Q''}$=(0,1)±$\boldsymbol{Q}$ should exist with opposite sign as shown in Fig. 2I (the same being true for $Im\tilde{O}_x(\boldsymbol{q}) + Im\tilde{O}_y(\boldsymbol{q})$). The second predicted characteristic is that the DW peaks at $\boldsymbol{Q}$ should exist clearly in $Re\tilde{O}_x(\boldsymbol{q}) - Re\tilde{O}_y(\boldsymbol{q})$ while their Bragg-satellite peaks at $\boldsymbol{Q'}$ = (1,0)±$\boldsymbol{Q}$ and $\boldsymbol{Q''}$=(0,1)±$\boldsymbol{Q}$ should disappear (the same being true for $Im\tilde{O}_x(\boldsymbol{q}) - Im\tilde{O}_y(\boldsymbol{q})$.) This is required because, if all O_y sites are multiplied by -1 as when we take the difference $Re\tilde{O}_x(\boldsymbol{q}) - Re\tilde{O}_y(\boldsymbol{q})$, a *d*-form factor IUC DW (Fig. 2I) is converted to a s'-form factor IUC DW (Fig. 2H). In that case, the signature of an IUCN-DW in $Re\tilde{O}_x(\boldsymbol{q}) - Re\tilde{O}_y(\boldsymbol{q})$ is that it should exhibit the characteristics of Fig. 2H (SI Section III).

Experimental Methods

To search for such phenomena, we use spectroscopic imaging STM (45) to measure both the differential tunneling conductance $g(\boldsymbol{r}, E = eV)$ and the tunnel-current magnitude $I(\boldsymbol{r}, E = eV)$, at bias voltage V, and on samples of both $Bi_2Sr_2CaCu_2O_{8+x}$ (BSCCO) and $Ca_{2-x}Na_xCuO_2Cl_2$ (NaCCOC). Because the electronic density-of-states $N(\vec{r}, E)$ enters as $g(\boldsymbol{r}, E) \propto \left[eI_s / \int_0^{eV_s} N(\boldsymbol{r}, E')dE'\right] N(\boldsymbol{r}, E)$ where I_s and V_s are arbitrary parameters, the unknown denominator $\int_0^{eV_s} N(\boldsymbol{r}, E')dE'$ always prevents valid determination of $N(\boldsymbol{r}, E)$ based only upon $g(\boldsymbol{r}, E)$ measurements. Instead, $Z(\boldsymbol{r}, |E|) = g(\boldsymbol{r}, E)/g(\boldsymbol{r}, -E)$ or $R(\boldsymbol{r}, |E|) = I(\boldsymbol{r}, E)/I(\boldsymbol{r}, -E)$, are used (11,12,13,43,45) in order to suppress the otherwise profound systematic errors. This approach allows distances, wavelengths, and phases of electronic structure to be measured correctly. Physically, the ratio $R(\boldsymbol{r}, V) \propto \int_o^{eV} N(\boldsymbol{r}, E)dE \,/\, \int_{-eV}^{0} N(\boldsymbol{r}, E)dE$ is measured using an identical tip-sample tunnel junction formed at $\boldsymbol{r}$ but using opposite bias voltage ±V ; it is a robust measure of the spatial symmetry of electronic states in the energy range |E|=eV. Additionally for this study, measurements at many pixels within each UC are required (to spatially discriminate every O_x , O_y and Cu site) while simultaneously

measuring in a sufficiently large FOV to achieve high resolution in phase definition (11,12, 44, 45).

Data acquired under these circumstance are shown in Figure 3A, the measured R($\boldsymbol{r}$, |E|=150meV) for a BSCCO sample with p=8±1%. This FOV contains ~ 15,000 each of individually resolved Cu, O_x and O_y sites. Figure 3B shows a magnified part of this R($\boldsymbol{r}$) with Cu sites indicated by blue dots; Figure 3C is the simultaneous topographic image showing how to identify the coordinate of each Cu, O_x and O_y site in all the images. Using the Lawler-Fujita phase-definition algorithm which was developed for IUC symmetry determination studies (12,44,45) we achieve a phase accuracy of $\sim 0.01\pi$ (44) throughout. As an example, Fig. 3D,E shows the segregation of measured $R(\boldsymbol{r})$ into two oxygen-site-specific images $O_x(\boldsymbol{r})$ and $O_y(\boldsymbol{r})$ from Fig. 3B (segregated Cu-site specific image is shown SI Section V). Larger FOV $O_x(\boldsymbol{r})$;$O_y(\boldsymbol{r})$ images segregated from $R(\boldsymbol{r})$ in Fig. 3A, and their Fourier transforms are shown in SI Section V.

Direct measurement of IUC DW Form-factor from Sublattice Phase-Resolved Images

Now we consider the complex Fourier transforms of $O_x(\boldsymbol{r})$ and $O_y(\boldsymbol{r})$, $\tilde{O}_x(\boldsymbol{q})$ and $\tilde{O}_y(\boldsymbol{q})$, as shown in Fig. 4A,B. We note that the use of $R(\boldsymbol{r},V)$ or $Z(\boldsymbol{r},V)$ is critically important for measuring relative phase of O_x/O_y sites throughout any IUC-DW, because analysis of $g(\boldsymbol{r},V)$ shows how the tip-sample junction establishment procedure (11,45) scrambles the IUC phase information irretrievably. Upon calculating the sum $Re\tilde{O}_x(\boldsymbol{q}) + Re\tilde{O}_y(\boldsymbol{q})$ as shown in Fig. 4C, we find no DW modulation peaks in the vicinity of $\boldsymbol{Q}$. Moreover there is evidence for a π-phase shift between much sharper peaks at **Q**' and **Q**'' (albeit with phase disorder). Both of these effects are exactly as expected for an IUCN-DW (see Fig. 2I). Further, the modulation peak at **Q** inside the first BZ that is weak in Figs. 4A and 4B and absent in Fig. 4C is strikingly visible in $Re\tilde{O}_x(\boldsymbol{q}) - Re\tilde{O}_y(\boldsymbol{q})$ as shown in Fig. 4D. Hence the absence of this feature in $Re\tilde{O}_x(\boldsymbol{q}) + Re\tilde{O}_y(\boldsymbol{q})$ cannot be

ascribed to broadness of the features surrounding $\boldsymbol{q} = 0$; rather, it is due to a virtually perfect phase cancelation of these peaks at **Q** (Fig 4C). Finally, the Bragg-satellite peaks at $\boldsymbol{Q'}$ = (1,0)±$\boldsymbol{Q}$ and $\boldsymbol{Q''}$=(0,1)±$\boldsymbol{Q}$ are absent in $Re\tilde{O}_x(\boldsymbol{q}) - Re\tilde{O}_y(\boldsymbol{q})$. Comparison of all these observations with predictions for an IUCN-DW in Fig. 2H,I, demonstrates that the modulations at $\boldsymbol{Q}$ maintain a phase difference of π between O_x and O_y within virtually every unit cell, and are therefore predominantly an IUC nematic DW exhibiting a *d*-form factor.

To demonstrate that these phenomena are not a specific property of a given tip-sample tunnel matrix element, or crystal symmetry, or surface termination layer, or cuprate material family, we carry out the identical analysis on data from NaCCOC samples with p=12±1% (SI Section V). For this compound, Fig. 4E,F are the measured $Re\tilde{O}_x(\boldsymbol{q})$ and $Re\tilde{O}_y(\boldsymbol{q})$. Again, the absence of DW peaks at $\boldsymbol{Q}$ in Fig. 4G which shows $Re\tilde{O}_x(\boldsymbol{q}) + Re\tilde{O}_y(\boldsymbol{q})$ are due to cancelation between O_x and O_y contributions, as these peaks are visible in$Re\tilde{O}_x(\boldsymbol{q})$ and $Re\tilde{O}_y(\boldsymbol{q})$ (Figs. 4E,F). Moreover, the sign change between the Bragg satellites $\boldsymbol{Q'}$ = (1,0)±$\boldsymbol{Q}$ and $\boldsymbol{Q''}$=(0,1)±$\boldsymbol{Q}$ in Fig. 4G exhibits a clear hallmark of an IUCN-DW. Finally $Re\tilde{O}_x(\boldsymbol{q}) - Re\tilde{O}_y(\boldsymbol{q})$ reveals again that the modulation peaks at **Q** inside the first BZ that are invisible Fig. 4G become vivid in Fig. 4H, while the Bragg-satellites disappear. One can see directly that these results are in comprehensive agreement with observations in Figs 4A-D meaning that the IUCN-DW of NaCCOC also exhibits a robustly *d*-symmetry form factor. This observation rules out experimental/materials systematics as the source of the IUCN-DW signal and therefore signifies that this state is a fundamental property of the underdoped CuO_2 plane.

Cuprate IUC Nematic DW is both Predominant and Robust

The dominance of the IUCN-DW can be quantified by measuring the *s*-, *s*'- and *d*-form factor components of the DW near $\boldsymbol{Q}$ inside the first BZ (SI Section II). In Fig. 5 we

show the power spectral density Fourier transform analysis only of Cu sites $|\tilde{C}_u(\boldsymbol{q})|^2$ (Fig 5A) to determine the *s*-form factor, and only at the O_x/O_y sites $|\left(\tilde{O}_x(\boldsymbol{q}) + \tilde{O}_y(\boldsymbol{q})\right)/2|^2$ for the *s*'-form factor (Fig. 5B) and $|\left(\tilde{O}_x(\boldsymbol{q}) - \tilde{O}_y(\boldsymbol{q})\right)/2|^2$ for the *d*-form factor (Fig. 5C) (SI Section II). The measured values are plotted along the dashed lines through $\boldsymbol{Q}$ in Fig. 5D and shows that the *d*-form factor component, manifest in $|\left(\tilde{O}_x(\boldsymbol{q}) - \tilde{O}_y(\boldsymbol{q})\right)/2|^2$, is far stronger than the others. This is also the case in the NaCCOC data (SI Section V). Figure 5E shows examples of measured complex valued $\tilde{O}_x(\boldsymbol{q}) \equiv Re\tilde{O}_x(\boldsymbol{q}) + iIm\tilde{O}_x(\boldsymbol{q})$ and compares them to $\tilde{O}_y(\boldsymbol{q}) \equiv Re\tilde{O}_y(\boldsymbol{q}) + iIm\tilde{O}_y(\boldsymbol{q})$ for each of a series of representative $\boldsymbol{q}$ within the DW peaks surrounding $\boldsymbol{Q}$ (all such data are from Figs 3,4). Figure 5F is a 2d-histogram showing both the magnitude and the phase difference between all such pairs $\tilde{O}_x(\boldsymbol{q})$: $\tilde{O}_y(\boldsymbol{q})$ whose $\boldsymbol{q}$ is within the same broad DW peaks (SI Section V). These data reveal the remarkably robust nature of the *d*-form factor of the IUCN-DW, and that the strong spatial disorder in DW modulations (e.g. Fig. 3A and Ref. 43) has little impact on the phase difference of π between O_x and O_y within every CuO_2 unit cell. Finally, focusing on specific regions of the R($\boldsymbol{r}$) images, one can now understand in microscopic detail how the well-known (11,13,43,45) but unexplained IUC spatial patterns of CuO_2 electronic structure (e.g. Fig. 5G) are formed. In fact, the virtually identical electronic structure patterns in BSCCO and NaCCOC (Fig. 5G) correspond to the instance in which an IUCN-DW occurs locally with $\boldsymbol{Q}$=(0.25,0) and with amplitude peaked on the central O_x sites (dashed vertical arrow). A model of a *d*-form factor IUC DW with this choice of spatial-phase is shown in Fig. 5H (SI Section I) with the calculated density adjacent; the agreement between data (Fig. 5G) and IUCN-DW model (Fig. 5H) is striking, giving a strong visual confirmation that the patterns observed in real space R($\boldsymbol{r}$) data are a direct consequence of an IUCN-DW.

Conclusions and Discussion

By generalizing our technique of phase-resolved intra-unit-cell electronic structure imaging at C_u, O_x, O_y (11,12,13,43,44,45), to include segregation of such data into three images ($C_u(\boldsymbol{r})$, $O_x(\boldsymbol{r})$, $O_y(\boldsymbol{r})$), sublattice-phase-resolved Fourier analysis yielding $\tilde{C}_u(\boldsymbol{q})$, $\tilde{O}_x(\boldsymbol{q})$and $\tilde{O}_y(\boldsymbol{q})$ becomes possible. Then, by comparing predicted signatures of an IUCN-DW in Figs. 2H,I with the equivalent measurements $Re\ \tilde{O}_x(\boldsymbol{q}) \pm Re\ \tilde{O}_y(\boldsymbol{q})$ in Fig. 4D,C and Fig. 4H,G, respectively, we find them in excellent agreement for both BSCCO and NaCCOC. Recently, Comin *et al* (20) have analyzed the polarization and angular dependence of the X-ray scattering cross-section of both underdoped $Bi_2Sr_2CuO_6$ and $YBa_2Cu_3O_7$. Using a model of the scattering amplitudes of the Cu and O atoms in the presence of charge-density modulations, they showed that a density wave that modulates IUC electronic structure with a *d*-form factor between O_x and O_y sites, provides a significantly better fit to the measured cross section than *s*- or *s*'-form factors. In our complementary approach, we demonstrate using direct sublattice-phase-resolved visualization that the DW consists of spatial modulations of the intra-unit-cell nematicity exhibiting a comprehensive and robust *d*-form factor. Therefore the microscopic structure of the cuprate density waves involves, predominantly, modulations of the IUC nematicity that maintain a relative phase of π between O_x and O_y. Moreover, the identification of this *d*-form factor IUCN-DW reveals a simple and harmonious explanation for the coexistence of what had been viewed as the dissimilar and distinct Q=0 nematic and Q≠0 DW broken symmetries in underdoped cuprates. Finally, the robustness of the intra-unit-cell phase difference of π, now demonstrated in both the Q=0 (12,13, SI Section V) and Q≠0 states (Fig. 5), implies that there must be a powerful and fundamentally important microscopic reason for universal inequivalence of electronic structure of the O_x and O_y sites in the pseudogap phase of underdoped cuprates.

Figure Captions

Figure 1 Intra-unit-cell Electronic Structure Symmetry in the CuO_2 Plane

A. Elementary C_u, O_x and O_y orbitals (sites) within the CuO_2 plane.
B. Schematic of uniform density on the Cu atoms (*s*-symmetry). The inactive O sites are now indicated by grey dots.
C. Schematic of uniform density on the O atoms (also an *s*-symmetry referred to here as extended-*s* or *s*'-symmetry). The inactive Cu sites are indicated by grey dots.
D. Schematic pattern with opposite-sign density on O_x and O_y (*d*-symmetry) as discussed in Ref. 12,45. The inactive Cu sites are indicated by grey dots.
E. Real component of Fourier transform of the *s*-symmetry IUC patterns derived only from Cu sublattice in (B) and with no DW modulation. The Bragg peaks have the same sign indicating the IUC states have s-symmetry.
F. Real component of Fourier transform of the ***s'***-symmetry patterns derived only from O_x and O_y sublattices in (C) and with no DW. The Bragg peaks are no longer within the CuO_2 reciprocal unit cell (RUC).
G. Fourier transform of the *d*-symmetry IUC patterns derived only from O_x and O_y sublattices as shown in (D) and with no DW modulation. The Bragg peaks now have the opposite sign indicating the IUC states have *d*-symmetry (12,45).

FIGURE 2 Types of CuO_2 Intra-unit-cell Density Waves

A. Spatial modulation with wavevector $\boldsymbol{Q}$=(Q,0) of the s-symmetry IUC patterns in (1B) is described by $S_{DW}(\boldsymbol{r}) = S\cos(\boldsymbol{Q}\cdot\boldsymbol{r_i})$; only Cu sites are active. The inactive O sites indicated by grey dots.

B. Spatial modulation with wavevector $\boldsymbol{Q}$ of the patterns in (1C) described by $S'_{DW}(\boldsymbol{r}) = S' \cos(\boldsymbol{Q} \cdot \boldsymbol{r_i})$; only O_x and O_y sites are active but they are always equivalent within each unit cell. The inactive Cu sites are indicated by grey dots.

C. Spatial modulation with wavevector $\boldsymbol{Q}$ of the patterns in (1D) described by $D_{DW}(\boldsymbol{r}) = D \cos(\boldsymbol{Q} \cdot \boldsymbol{r_i})$; only O_x and O_y sites are relevant but now they are always inequivalent and indeed π out of phase.

D. $Re\tilde{S}_{DW}(\boldsymbol{q})$, the real-component of Fourier transform of the pattern in (2A). For this s-form factor DW, the DW satellites of inequivalent Bragg peaks $\boldsymbol{Q}$' and $\boldsymbol{Q}$'' exhibit same sign.

E. $Re\tilde{S'}_{DW}(\boldsymbol{q})$, the real-component of Fourier transform of the pattern in (2B). For this s'-form factor DW, the peaks at $\boldsymbol{Q}$ are clear and the actual Bragg peaks of (2B) are outside the RUC of CuO_2.

F. $Re\widetilde{D}_{DW}(\boldsymbol{q})$, the real-component of Fourier transform of the pattern in (2C). For this d-form factor DW, the DW Bragg-satellites peaks at $\boldsymbol{Q}$' and $\boldsymbol{Q}$'' exhibit opposite sign. More profoundly, because they are out of phase by π the contributions of O_x and O_y *sites* in each unit cell cancel, resulting in the disappearance of the DW modulation peaks $\boldsymbol{Q}$ within the BZ (dashed box).

G. $Re\tilde{S}_{DW}(\boldsymbol{q})$ expected for an IUC DW with *s*-form factor having modulations along both x- and y-axes at $\boldsymbol{Q}$=(Q,0);(0,Q) (SI Section III); the DW satellites of inequivalent Bragg peaks $\boldsymbol{Q}$' and $\boldsymbol{Q}$'' exhibit same sign and the basic modulations at $\boldsymbol{Q}$ are clear.

H. $Re\tilde{S'}_{DW}(\boldsymbol{q})$ expected for an IUC DW with *s'*-form factor having modulations at $\boldsymbol{Q}$=(Q,0);(0,Q) (SI Section III) ; the Bragg-satellite peaks are outside the CuO2 RUC but modulation peaks at $\boldsymbol{Q}$ are clear.

I. $Re\widetilde{D}_{DW}(\boldsymbol{q})$ expected for an IUC DW with *d*-form factor having modulations at $\boldsymbol{Q}$=(Q,0);(0,Q) (SI Section III); the DW satellites of inequivalent Bragg peaks

Q' and ***Q***'' exhibit opposite sign, and the basic DW modulation peaks ***Q*** have disappeared from within the BZ.

Figure 3 Oxygen-site-specific Imaging and Segregation of R(*r*)

A. Measured R(***r***) with ~16 pixels within each CuO_2 unit cell and ~45 nm square FOV for BSCCO sample with p~8+-1%. This R(***r***) electronic structure image reveals extensive Q=0 IUC nematic order (12,13) (SI Section V).
B. Smaller section of R(***r***) in FOV of 3A, now showing the location of the Cu lattice as blue dots. The well known (11,12,13,45) breaking of rotational symmetry within virtually every CuO_2 unit cell, or IUC nematicity, and the modulations thereof, are obvious.
C. Topographic image of FOV in 3B showing Cu lattice sites as identified from the Bi atom locations as blue dots. By using the Lawler-Fujita algorithm (12,44) spatial-phase accuracy for the CuO_2 plane of ~0.01π is achieved throughout .
D. In the same FOV as 3B, we measure the value of R at every O_x site and show the resulting function O_x(***r***).
E. In the same FOV as 3B, we measure the value of R at every O_y site and show the resulting function O_y(***r***).

Figure 4 Sublattice Phase-resolved Fourier Analysis yields IUC Nematic DW

A. Measured $Re\tilde{O}_x(\boldsymbol{q})$ from R(***r***) in 3A; the four DW peaks at ***Q***, and the DW Bragg-satellite peaks exist but are all poorly resolved.
B. $Re\tilde{O}_y(\boldsymbol{q})$ from 3A; the four DW peaks at ***Q***, and the DW Bragg-satellite peaks exist but are all poorly resolved.
C. Measured $Re\tilde{O}_x(\boldsymbol{q}) + Re\tilde{O}_y(\boldsymbol{q})$ from A,B. The four DW peaks at ***Q*** are not detectable while the DW Bragg-satellite peaks are enhanced and clarified.

Comparing to Fig. 2I these are the expected phenomena of an IUC nematic DW (with spatial disorder in the DW).

D. Measured $Re\tilde{O}_x(\boldsymbol{q}) - Re\tilde{O}_y(\boldsymbol{q})$ from A,B. The four DW peaks at ***Q*** are strongly enhanced while the DW Bragg-satellite peaks have disappeared. Comparing to Fig. 2H, these are once again the expected phenomena of a IUC nematic DW.

E. Measured $Re\tilde{O}_x(\boldsymbol{q})$ for NaCCOC sample with p~12+-1%; the DW peaks at ***Q***, and the DW Bragg-satellite peaks exist but are poorly resolved.

F. Measured $Re\tilde{O}_y(\boldsymbol{q})$ for NaCCOC; the DW peaks at ***Q***, and the DW Bragg-satellite peaks exist but are poorly resolved.

G. Measured $Re\tilde{O}_x(\boldsymbol{q}) + Re\tilde{O}_y(\boldsymbol{q})$ from E,F. The four DW peaks at ***Q*** are no longer detectable while the DW Bragg-satellite peaks are enhanced and clarified. Importantly (modulo some phase noise) the Bragg-satellite peaks at inequivalent ***Q***' and ***Q***'' exhibit opposite sign. Comparing to Fig. 2I these are the expected phenomena of a IUCN- DW.

H. Measured $Re\tilde{O}_x(\boldsymbol{q}) - Re\tilde{O}_y(\boldsymbol{q})$ from E,F. The four DW peaks at ***Q*** are enhanced while the DW Bragg-satellite peaks have disappeared. Comparing to Fig. 2H these confirm the IUCN- DW conclusion.

Figure 5 IUC Nematic DW: Predominance and Robustness

A. PSD Fourier transforms of R(***r***) measured only at Cu sites $|\tilde{C}_u(\boldsymbol{q})|^2$; this provides the quantitative measure of s-form factor in the IUC DW.

B. PSD Fourier transforms of R(***r***) measured only at only at the O_x/O_y sites yielding $|\left(\tilde{O}_x(\boldsymbol{q}) + \tilde{O}_y(\boldsymbol{q})\right)/2|^2$. This provides the measure of relative strength of the s'-form factor in the IUC DW.

C. PSD Fourier transforms of R(***r***) measured only at only at the O_x/O_y sites yielding $|\left(\tilde{O}_x(\boldsymbol{q}) - \tilde{O}_y(\boldsymbol{q})\right)/2|^2$. This provides the measure of relative strength of the *d*-form factor in the IUC DW.

D. Measured PSD is plotted along the dashed line through ***Q*** in Fig. 5A,B,C and shows the *d*-form factor component predominates greatly. The measured ratios within the DW peaks surrounding ***Q*** is *d/s* > 5 and *d/s'* > 12.

E. $\tilde{O}_x(\boldsymbol{q}) \equiv Re\tilde{O}_x(\boldsymbol{q}) + iIm\tilde{O}_x(\boldsymbol{q})$ compared to $\tilde{O}_y(\boldsymbol{q}) \equiv Re\tilde{O}_y(\boldsymbol{q}) + iIm\tilde{O}_y(\boldsymbol{q})$ for each of a series of representative ***q*** within the DW peaks surrounding ***Q***. This shows how, wherever the CuO_2 unit cell resides in the disordered DW (Fig 3A), the relative phase between the O_x and O_y sites is very close to π while the difference in magnitudes are close to zero.

F. Two-axis histogram of difference in normalized magnitude (vertical) and phase (horizontal) between all pairs $\tilde{O}_x(\boldsymbol{r},\boldsymbol{Q})$ and $\tilde{O}_y(\boldsymbol{r},\boldsymbol{Q})$ which are obtained by Fourier filtration of $O_x(\boldsymbol{r})$ and $O_y(\boldsymbol{r})$ to retain only ***q***~***Q*** (SI Section V). This represents the measured distribution of amplitude difference, and phase difference, between each pair of O_x /O_y sites everywhere in the DW, It demonstrates directly that their relative phase is always close to π and that their magnitude differences are always close to zero.

G. Measured R(***r***) images of local electronic structure patterns that commonly occur in BSCCO and NaCCOC (11). The Cu and O_x sites (as labeled by solid and dashed arrows respectively) were determined independently and directly from topographic images.(11)

H. IUCN-DW model with **Q**=(0.25,0) and amplitude maximum on the central O_x site (dashed arrow); the calculated charge density pattern from this model is shown adjacent. Therefore an IUCN-DW model with this particular spatial-phase provides an apparently excellent explanation for the observed density patterns shown in G and reported previously in Refs 11,12,13,45.

I. Acknowledgements

We acknowledge and thank S. Billinge, R. Comin, A. Damascelli, D.-H. Lee, S.A. Kivelson, A. Kostin, and A.P. Mackenzie, for very helpful discussions and communications. Experimental studies were supported by the Center for Emergent Superconductivity, an Energy Frontier Research Center, headquartered at Brookhaven National Laboratory and funded by the U.S. Department of Energy under DE-2009-BNL-PM015, as well as by a Grant-in-Aid for Scientific Research from the Ministry of Science and Education (Japan) and the Global Centers of Excellence Program for Japan Society for the Promotion of Science. C. K. K. acknowledges support from the *Fluct Team* program at Brookhaven National Laboratory under contract DE-AC02-98CH10886. S.D.E. acknowledges the support of EPSRC through the Programme Grant 'Topological Protection and Non-Equilibrium States in Correlated Electron Systems". Y.K. acknowledges support form studies at RIKEN by JSPS KAKENHI (19840052, 20244060). Theoretical studies at Cornell University were supported by NSF Grant DMR-1120296 to the Cornell Center for Materials Research and by NSF Grant DMR-0955822. A.A. and S.S. are supported by NSF Grant DMR-1103860 and by the Templeton Foundation.

References

1 Orenstein J, Millis AJ (2000) Advances in the physics of high-temperature superconductivity. *Science* 288(5465):468—474.

2 Timusk T, Statt B (1999) The pseudogap in high-temperature superconductors: An experimental survey. *Rep Prog Phys* 62(1):61—122.

3 Emery VJ (1987) Theory of high-T_c superconductivity in oxides. *Phys Rev Lett* 58(26)**:**2794—2797.

4 Varma CM, Schmitt-Rink S, Abrahams E (1987) Charge transfer excitations and superconductivity in "ionic" metals. *Solid State Comm* 62(10):681-685.

5 Sachdev S, Read N (1991) Large N expansion for frustrated and doped quantum antiferromagnets. *Int J Mod Phys B* 5(1):219-249.

6 Vojta M, Sachdev S (1999) Charge order, superconductivity, and a global phase diagram of doped antiferromagnets. *Phys Rev Lett* 83(19):3916—3919.

7 Kivelson SA, Fradkin E, Geballe TH (2004) Quasi-one-dimensional dynamics and a nematic phases in two-dimensional Emery model. *Phys Rev B* 69(14):144505-1—144505-7.

8 Fisher MH, Kim E-A (2011) Mean-field analysis of intra-unit-cell order in the Emery model of the CuO_2 plane. *Phys Rev B* 84(14):144502-1—144502-10.

9 Varma C (1997) Non-Fermi-liquid states and pairing instability of a general model of copper oxide metals. *Phys Rev B* 55(21):14554—14580.

10 Kohsaka Y, et al. (2012) Visualization of the emergence of the pseudogap state and the evolution to superconductivity in a lightly hole-doped Mott insulator. *Nat Phys* 8(7):534—538.

11 Kohsaka Y, et al. (2007) An intrinsic bond-centered electronic glass with unidirectional domains in underdoped cuprates. *Science* 315(5817):1380—1385.

12 Lawler MJ, et al. (2010) Intra-unit-cell electronic nematicity of the high-T_c copper-oxide pseudogap states. *Nature* 466(7304)**:**347—351.

[13] Fujita K., *et al* (2014) Simultaneous Transitions in Cuprate Momentum-Space Topology and Electronic Symmetry Breaking. Preprint available at http://arxiv.org/abs/1403.7788

[14] Fauqué B, et al. (2006) Magnetic order in the pseudogap phase of high-T_c superconductors. *Phys Rev Lett* 96(19):197001-1—197001-4.

[15] Li Y, et al. (2008) Unusual magnetic order in the pseudogap region of the superconductor $HgBa_2CuO_{4+\delta}$. *Nature* 455(7211):372—375.

[16] Almeida-Didry SD, et al. (2012) Evidence for intra-unit-cell magnetic order in $Bi_2Sr_2CaCu_2O_{8+\delta}$. *Phys Rev B* 86(2):020504-1—020504-4.

[17] Xia J, et al. (2008) Polar Kerr-effect measurements of the high-temperature $YBa_2Cu_3O_{6+x}$ superconductor: Evidence for broken symmetry near the pseudogap temperature. *Phys Rev Lett* 100(12):127002-1—127002-4.

[18] Daou, R. et al. (2010) Broken rotational symmetry in the pseudogap phase of a high-Tc superconductor *Nature* 463, 519-523

[19] Achkar AJ, et al. (2013) Resonant X-ray scattering measurements of a spatial modulation of the Cu 3*d* and O 2*p* energies in stripe-ordered cuprate superconductors. *Phys Rev Lett* 110(1):017001-1—017001-5.

[20] Comin R, et al. (2014) The symmetry of charge order in cuprates. Preprint available arXiv:1402.5415.

[21] Tranquada JM, et al. (1996) Neutron-scattering study of stripe-phase order of holes and spins in $La_{1.48}Nd_{0.4}Sr_{0.12}CuO_4$. *Phys Rev B* 54(10):7489—7499.

[22] Kim YJ, Gu GD, Gog T, Casa D (2008) X-ray scattering study of charge density waves in $La_{2-x}Ba_xCuO_4$. *Phys Rev B* 77(6):064520-1—064520-10.

[23] Chang J, et al. (2012) Direct observation of competition between superconductivity and charge density wave order in $YBa_2Cu_3O_{6.67}$. *Nat Phys* 8(12):871—876.

[24] Ghiringhelli G, et al. (2012) Long-range incommensurate charge fluctuations in $(Y,Nd)Ba_2Cu_3O_{6+x}$. *Science* 337(6096):821—825.

[25] Achkar AJ, et al. (2012) Distinct charge orders in the planes and chains of ortho-III-ordered $YBa_2Cu_3O_{6+\delta}$ superconductors identified by resonant elastic X-ray scattering. *Phys Rev Lett* 109(16):167001-1—167001-5.

[26] Torchinsky DH, Mahmood F, Bollinger AT, Božović I, Gedik N (2013) Fluctuating charge-density waves in a cuprate superconductor. *Nat Mat* 12(5):387—391

[27] Blackburn E, et al. (2013) X-ray diffraction observations of a charge-density-wave order in superconducting ortho-II $YBa_2Cu_3O_{6.54}$ single crystals in zero magnetic field. *Phys Rev Lett* 110(13):137004-1—137004-5.

[28] Hinton JP, et al. (2013) New collective mode in $YBa_2Cu_3O_{6+x}$ observed by time-domain reflectometry. *Phys Rev B* 88(6)**:**060508-1—060508-5.

[29] Comin R, et al. (2014) Charge order driven by Fermi-arc instability in $Bi_2Sr_{2-x}La_xCuO_{6+\delta}$. *Science* 343(6169):390—392.

[30] da Silva Neto EH, et al. (2014) Ubiquitous interplay between charge ordering and high-temperature superconductivity in cuprates. *Science* 343(6169):393—396.

[31] Hoffman JE, et al. (2002) A four unit cell periodic pattern of quasi-particle states surrounding vortex cores in $Bi_2Sr_2CaCu_2O_{8+\delta}$. *Science* 295(5554):466—469.

[32] Li J-X, Wu C-Q, Lee D-H (2006) Checkerboard charge density wave and pseudogap of high-T_c cuprate. *Phys Rev B* 74(18):184515-1—184515-6.

[33] Seo K, Chen H-D, Hu J (2007) *d*-wave checkerboard order in cuprates. *Phys Rev B* 76(2):020511-1—020511-4.

[34] Newns DM, Tsuei CC (2007) Fluctuating Cu-O-Cu bond model of high-temperature superconductivity. *Nat Phys* 3(3):184-191.

[35] Honerkamp C, Fu HC, Lee D-H (2007) Phonons and *d*-wave pairing in the two-dimensional Hubbard model. *Phys Rev B* 75(1):014503-1—014503-5.

[36] Metlitski MA, Sachdev S (2010) Instabilities near the onset of spin density wave order in metals. *New J Phys* 12(10):105007-1—105007-13.

[37] Holder T, Metzner W (2012) Incommensurate nematic fluctuations in two-dimensional metals. *Phys Rev B* 85(16):165130-1—165130-7.

[38] Efetov KB, Meier H, Pépin C (2013) Pseudogap state near a quantum critical point. *Nat*

Phys 9(7):442—446.

[39] Bulut S, Atkinson WA, Kampf AP (2013) Spatially modulated electronic nematicity in the three-band model of cuprate superconductors. *Phys Rev B* 88(15):155132-1—155132-13.

[40] Sachdev S, La Placa R (2013) Bond order in two-dimensional metals with antiferromagnetic exchange interactions. *Phys Rev Lett* 111(2):027202-1—027202-5.

[41] Davis JC, Lee D-H (2013) Concepts relating magnetic interactions, intertwined electronic orders, and strongly correlated superconductivity. *Proc Nat Acad Sci* 110(44)**:**17623—17630.

[42] Allais A, Bauer J, Sachdev S (2014) Bond order instabilities in a correlated two-dimensional metal. arXiv:1402.4807.

[43] Mesaros A, et al. (2011) Topological defects coupling smectic modulations to intra-unit-cell nematicity in cuprates. *Science* 333(6041):426—430.

[44] Hamidian M, et al. (2012) Picometer registration of zinc impurity states in $Bi_2Sr_2CaCu_2O_{8+\delta}$ for phase determination in intra-unit-cell Fourier transform STM. *New J Phys* 14(5):053017-1—053017-13

[45] Fujita K, et al. (2011) Spectroscopic imaging scanning tunneling microscopy studies of electronic structure in the superconducting and pseudogap phases of cuprate high-T_c superconductors. *J Phys Soc Jpn* 81(1):011005-1—011005-17.

FIG1

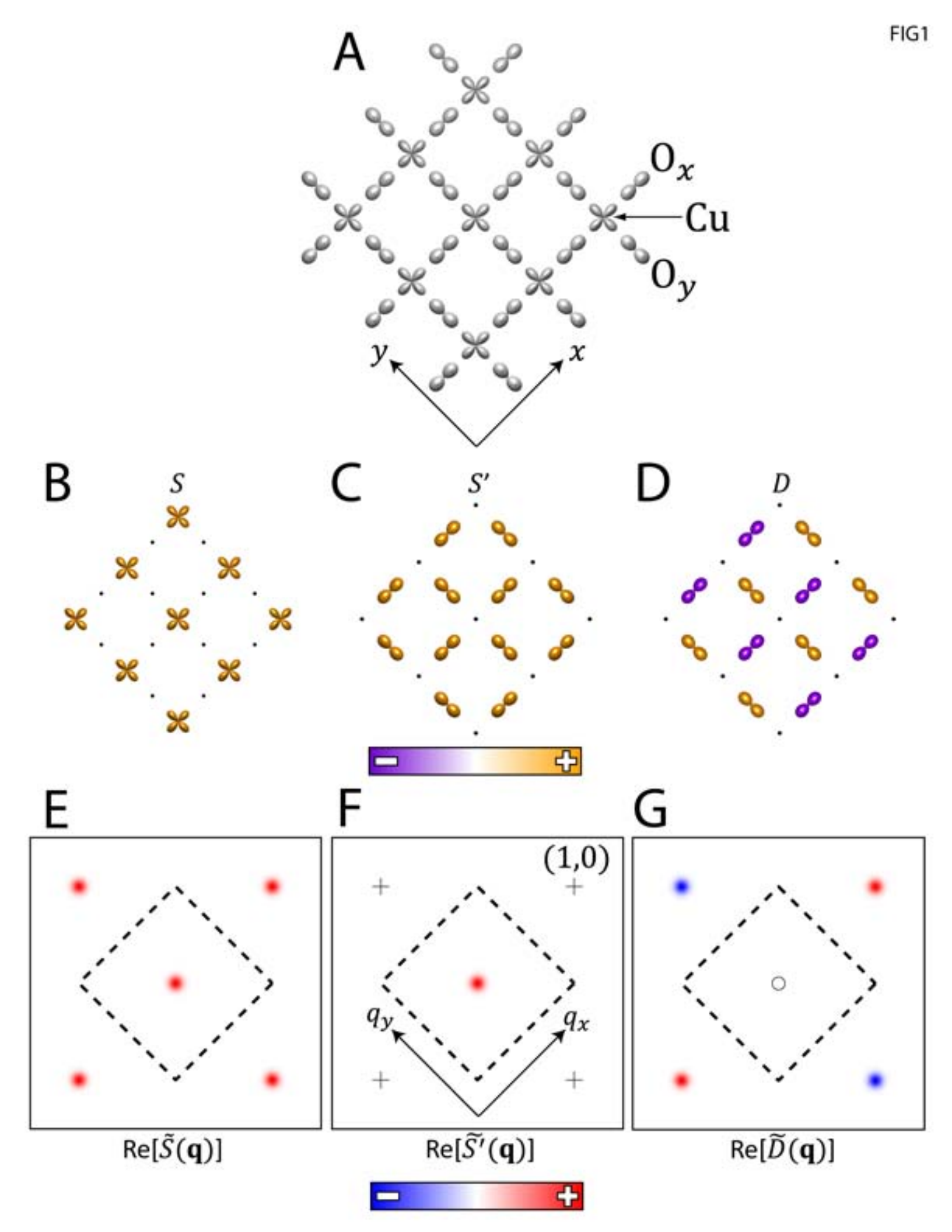
A
O_x
Cu
O_y
y
x
B
S
C
S′
D
D
E
F
G
(1,0)
q_y
q_x
$\mathrm{Re}[\tilde{S}(\mathbf{q})]$
$\mathrm{Re}[\tilde{S}'(\mathbf{q})]$
$\mathrm{Re}[\tilde{D}(\mathbf{q})]$

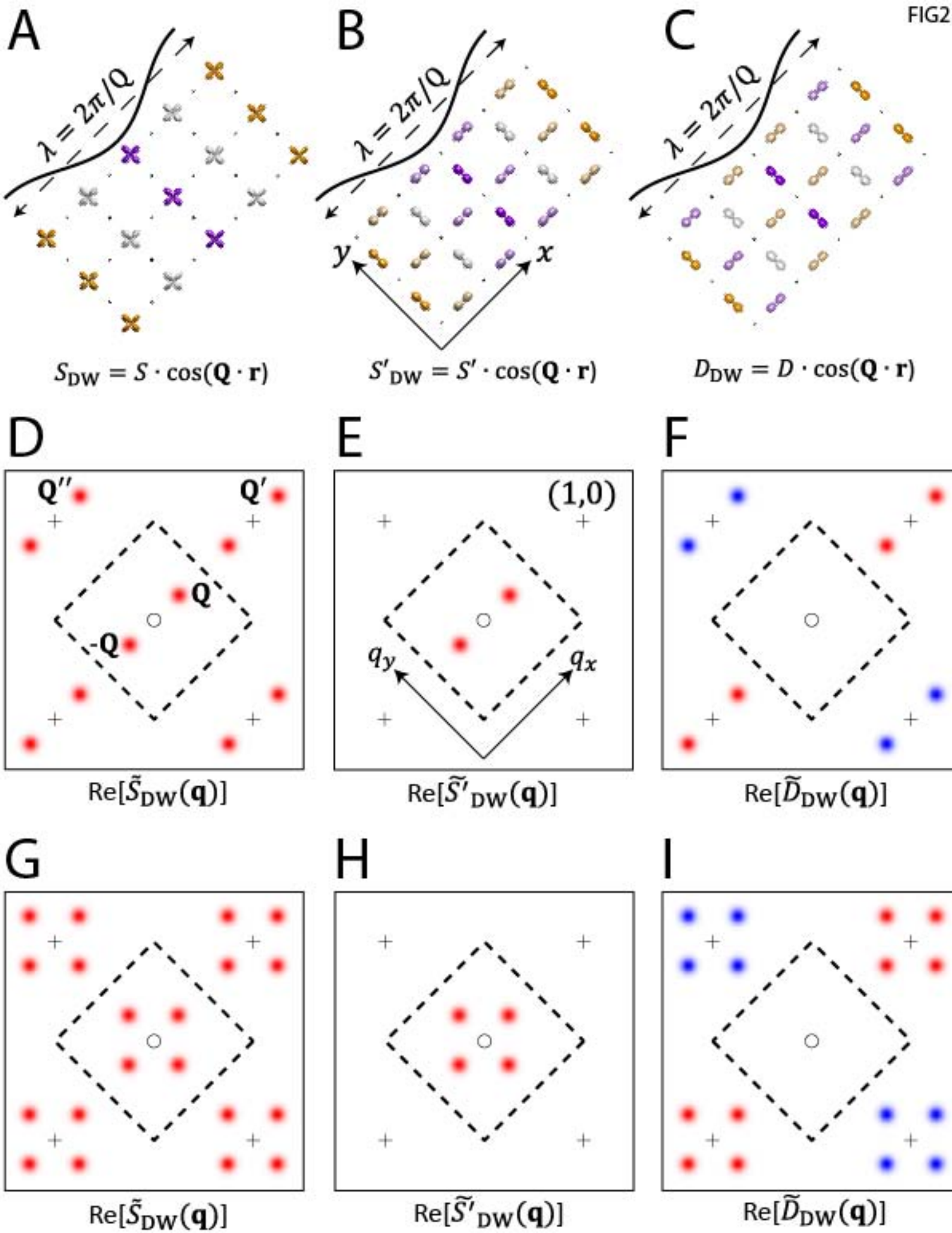
A
B
C
$\lambda = 2\pi/Q$
$\lambda = 2\pi/Q$
$\lambda = 2\pi/Q$
y
x
$S_{DW} = S \cdot \cos(\mathbf{Q} \cdot \mathbf{r})$
$S'_{DW} = S' \cdot \cos(\mathbf{Q} \cdot \mathbf{r})$
$D_{DW} = D \cdot \cos(\mathbf{Q} \cdot \mathbf{r})$
D
E
F
$\mathbf{Q}''$
$\mathbf{Q}'$
$\mathbf{Q}$
$-\mathbf{Q}$
(1,0)
q_y
q_x
$\mathrm{Re}[\tilde{S}_{DW}(\mathbf{q})]$
$\mathrm{Re}[\tilde{S}'_{DW}(\mathbf{q})]$
$\mathrm{Re}[\tilde{D}_{DW}(\mathbf{q})]$
G
H
I
$\mathrm{Re}[\tilde{S}_{DW}(\mathbf{q})]$
$\mathrm{Re}[\tilde{S}'_{DW}(\mathbf{q})]$
$\mathrm{Re}[\tilde{D}_{DW}(\mathbf{q})]$

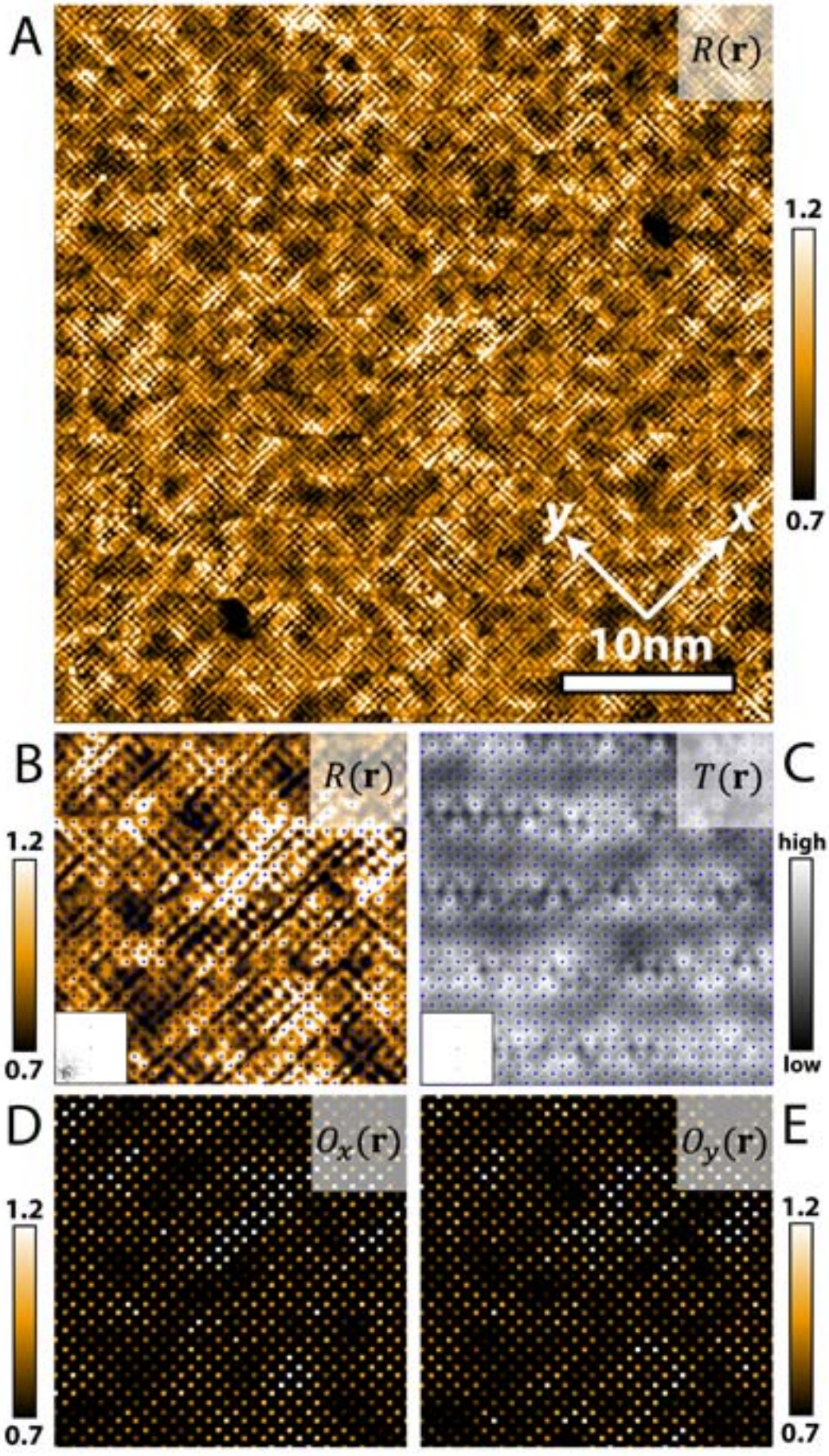
A
$R(\mathbf{r})$
1.2
0.7
y
x
10nm
B
$R(\mathbf{r})$
1.2
0.7
C
$T(\mathbf{r})$
high
low
D
$O_x(\mathbf{r})$
1.2
0.7
E
$O_y(\mathbf{r})$
1.2
0.7

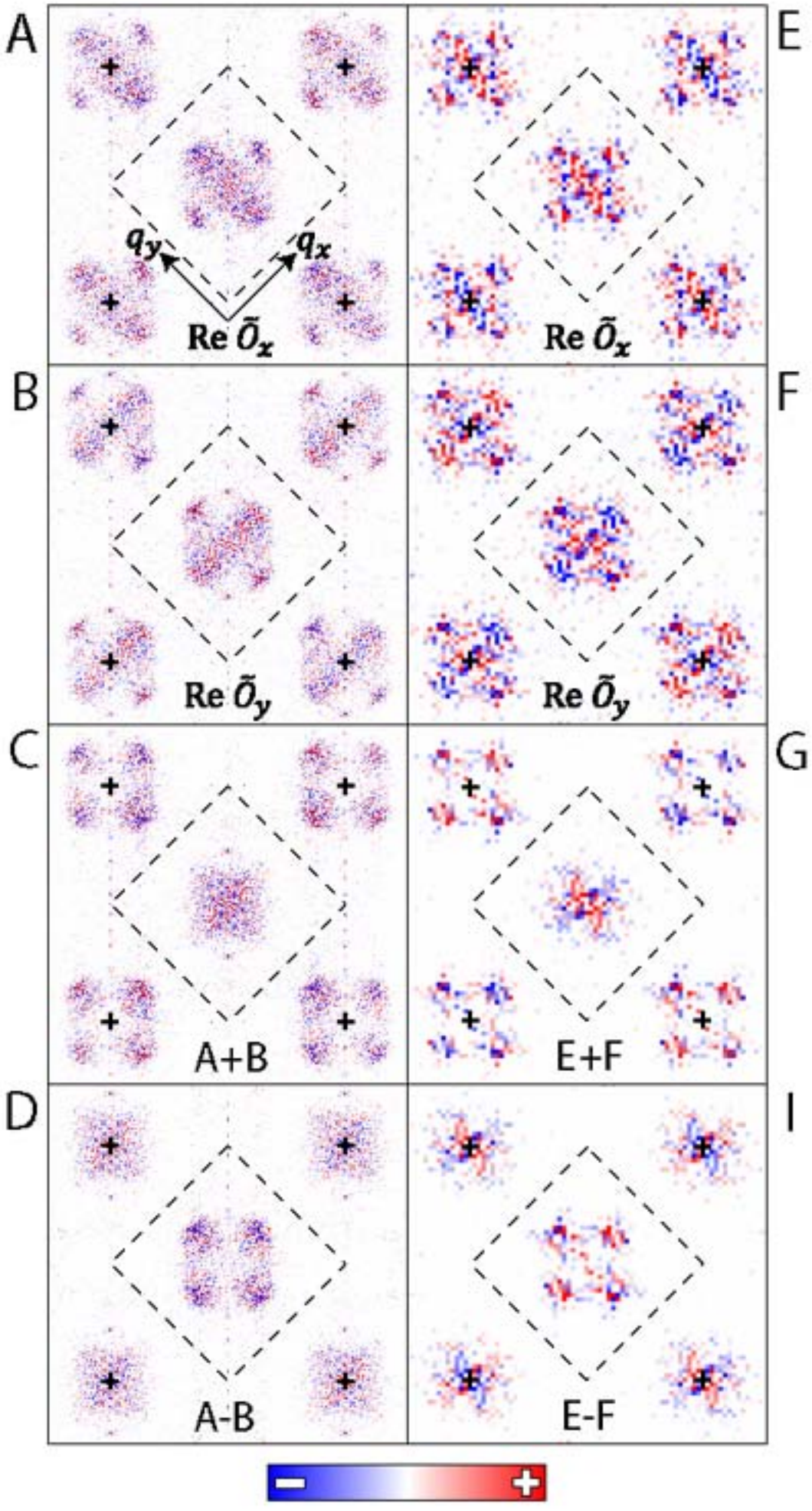
A
E
q_y
q_x
Re $\tilde{O}_x$
Re $\tilde{O}_x$
B
F
Re $\tilde{O}_y$
Re $\tilde{O}_y$
C
G
A+B
E+F
D
I
A-B
E-F
−
+

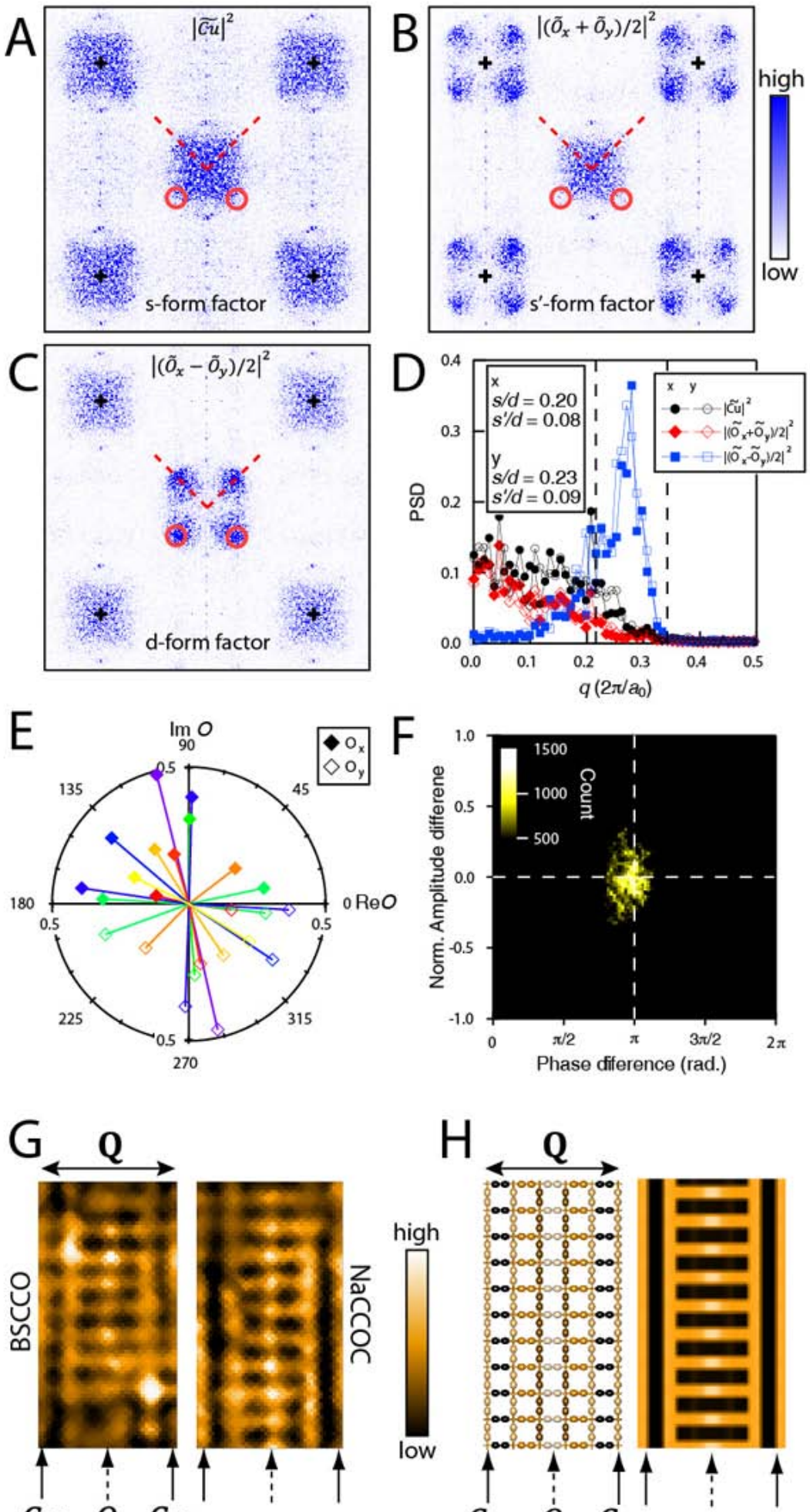
A
$|\widetilde{Cu}|^2$
s-form factor
B
$|(\tilde{O}_x + \tilde{O}_y)/2|^2$
s'-form factor
high
low
C
$|(\tilde{O}_x - \tilde{O}_y)/2|^2$
d-form factor
D
x
s/d = 0.20
s'/d = 0.08
y
s/d = 0.23
s'/d = 0.09
x y
$|\widetilde{Cu}|^2$
$|(\widetilde{O}_x+\widetilde{O}_y)/2|^2$
$|(\widetilde{O}_x-\widetilde{O}_y)/2|^2$
PSD
q (2π/a0)
E
Im O
Re O
Ox
Oy
F
Norm. Amplitude differene
Phase diference (rad.)
Count
G
Q
BSCCO
NaCCOC
Cu O Cu
H
Q
high
low
Cu O Cu

Supporting Information For

Intra-unit-cell Nematic Density Wave: Unfied Broken Symmetry of the Cuprate Pseudogap State

K. Fujita†, M. H. Hamidian†, S. D. Edkins, Chung Koo Kim, Y. Kohsaka,
M. Azuma, M. Takano, H. Takagi, H. Eisaki, S. Uchida, A. Allais,
M. J. Lawler, E. -A. Kim, Subir Sachdev & J. C. Séamus Davis

I Models of spatially modulated order in underdoped cuprates

The study of the underdoped cuprates has led to proposals of a large number of density-wave orders with non-trivial form factors [1]-[33]. Here we provide a unified perspective on these orders, while highlighting the key characteristics detected by our observations.

It is useful to begin by considering the following bi-local observable at the Cu sites $\boldsymbol{r_i}$ and $\boldsymbol{r_j}$ [21, 22]

$$\langle c^{\dagger}_{i\alpha} c_{j\alpha} \rangle = \sum_{\boldsymbol{Q}} \left[\sum_{\boldsymbol{k}} P(\boldsymbol{k}, \boldsymbol{Q}) e^{i\boldsymbol{k}\cdot(\boldsymbol{r_i}-\boldsymbol{r_j})} \right] e^{i\boldsymbol{Q}\cdot(\boldsymbol{r_i}+\boldsymbol{r_j})/2} \tag{1.1}$$

where $c_{i\alpha}$ annihilates an electron with spin α on a site a position $\boldsymbol{r_i}$. The wavevector $\mathbf{Q}$ is associated with a modulation in the *average* co-ordinate $(\boldsymbol{r_i} + \boldsymbol{r_j})/2$. The interesting form-factor is the dependence on the *relative* co-ordinate $\boldsymbol{r_i} - \boldsymbol{r_j}$. An advantage of the formulation in Eq. (1.1) is that it provides a very efficient characterization of symmetries. Hermiticity of the observable requires that

$$P^*(\boldsymbol{k}, \boldsymbol{Q}) = P(\boldsymbol{k}, -\boldsymbol{Q}) \tag{1.2}$$

while

$$P(\boldsymbol{k}, \boldsymbol{Q}) = P(-\boldsymbol{k}, \boldsymbol{Q}) \tag{1.3}$$

if time-reversal symmetry is preserved.

A number of other studies [1, 4, 16, 17,19] have made the closely related, but distinct parameterization

$$\langle c^{\dagger}_{i\alpha} c_{j\alpha} \rangle = \sum_{\boldsymbol{Q}} \left[\sum_{\boldsymbol{k}} f(\boldsymbol{k}, \boldsymbol{Q}) e^{i\boldsymbol{k}\cdot(\boldsymbol{r_i}-\boldsymbol{r_j})} \right] e^{i\boldsymbol{Q}\cdot\boldsymbol{r_i}} \tag{1.4}$$

and then considered various ansatzes for the function $f(\mathbf{k},\mathbf{Q})$. These are clearly related to those for $P(\mathbf{k},\mathbf{Q})$ by

$$f(\boldsymbol{k}, \boldsymbol{Q}) = P(\boldsymbol{k} + \frac{\boldsymbol{Q}}{2}, \boldsymbol{Q}) \tag{1.5}$$

It is now clear that the relations (1.2) and (1.3) take a more complex form in terms of $f(\boldsymbol{k},\boldsymbol{Q})$. Also, a d-wave form factor for $f(\boldsymbol{k},\boldsymbol{Q})$ is *not* equal to a d-wave form factor for $P(\boldsymbol{k},\boldsymbol{Q})$**,** except at $\boldsymbol{Q}=0$.

We conduct the remainder of the discussion using $P(\boldsymbol{k},\boldsymbol{Q})$ and Eq. (1.1). Depending upon the value of **Q**, various crystalline symmetries can also place restrictions on $P(\boldsymbol{k},\boldsymbol{Q})$, and we illustrate this with a few examples.

An early discussion of a state with non-trivial form factors was the "staggered flux" state (also called the "d-density wave" state), which carries spontaneous staggered currents [2]-[6]. This state has $P(\boldsymbol{k},\boldsymbol{Q})$ non-zero only for **Q**=(π,π), and

$$P(\boldsymbol{k},\boldsymbol{Q}) = P_{sf}\big(\sin(k_x)-\sin(k_y)\big) + P'_{sf}\big(\sin(2k_x)-\sin(2k_y)\big)+\cdots \qquad (1.6)$$

where P_{sf}, P'_{sf} are constants. All terms on the right-hand-side are required by symmetry to be odd under time-reversal (*i.e.* odd in **k**), and odd under the interchange $k_x \leftrightarrow k_y$. In the present notation, therefore, the staggered-flux state is a p-density wave. Please note that a d-wave form factor in our notation refers to a distinct state below, which should *not* be confused with the "d-density wave" of Refs. [2]-[6]. With $P(\boldsymbol{k},\boldsymbol{Q})$ non-zero only for **Q**=0 and odd in **k**, we obtain states with spontaneous uniform currents [7].

Another much-studied state is the electronic nematic [8]-[10]. This has $P(\boldsymbol{k},\boldsymbol{Q})$ non-zero only for **Q**=0, with

$$P(\boldsymbol{k},\boldsymbol{Q}) = P_{n}\big(\cos(k_x)-\cos(k_y)\big) + P'_{n}\big(\cos(2k_x)-\cos(2k_y)\big)+\cdots \qquad (1.7)$$

Now all terms on the right-hand-side should be even in **k**, and odd under the interchange $k_x \leftrightarrow k_y$. The ansatz in Eq. (1.7) also applies to "incommensurate nematics" [21]-[31] which have $P(\boldsymbol{k},\boldsymbol{Q})$ non-zero only for $\boldsymbol{Q}=(\pm Q_0,\pm Q_0)$: these are density waves with **Q** along the diagonals of the square lattice Brillouin zone, and a purely d-wave form factor.

Finally, we turn to the density waves considered in our manuscript. These have $P(\boldsymbol{k},\boldsymbol{Q})$ non-zero only for $\boldsymbol{Q}=(0,\pm Q_0)$ and $(\pm Q_0,0)$. We assume they preserve time-reversal, and then the form-factor has the general form [22]

$$P(\boldsymbol{k},\boldsymbol{Q}) = P_s + P_{s'}\big(\cos(k_x)+\cos(k_y)\big) + P_d\big(\cos(k_x)-\cos(k_y)\big)+\cdots \qquad (1.8).$$

For general incommensurate Q_0, any even function of k_x is allowed on the right-hand-side. Using arguments based upon instabilities of metals with local antiferromagnetic correlations, it was argued in Ref. [22] that such a density wave is predominantly d-wave *i.e.* $|P_{\rm d}| \gg P_{\rm s}$ and $|P_{\rm d}| \gg P_{\rm s'}$, so that it is very nearly, but not exactly, an incommensurate nematic. The d-wave-ness here is a statement about the physics of the local electronic correlations, and is not fully determined by symmetry.

We now make contact with the local observables considered in SI section II and III and as measured by STM. Via the canonical transformation from the two-band to the single-band model of the CuO_2 layer, we can deduce the general relationship

$$\langle c_{i\alpha}^{\dagger} c_{j\alpha} + c_{j\alpha}^{\dagger} c_{i\alpha} \rangle = \begin{cases} \frac{1}{K} n(\boldsymbol{r_{Cu}}) \text{ for } i = j \\ \frac{1}{K'} n(\boldsymbol{r_{O_x}}) \text{ for } i,j \text{ n.n along x-direction} \\ \frac{1}{K'} n\left(\boldsymbol{r_{O_y}}\right) \text{ for } i,j \text{ n.n along y-direction} \end{cases} \quad (1.9).$$

Here $n(\mathbf{r})$ is any density-like (*i.e.* invariant under time-reversal and spin rotations) observable and K,K' are proportionality constants. Combining (1.1) (1.8) (1.9) we can now write

$$n(\boldsymbol{r_{Cu}}) = 2K\mathrm{Re}\left\{[\textstyle\sum_k P(\boldsymbol{k},\boldsymbol{Q})]e^{i\boldsymbol{Q}\cdot\boldsymbol{r_{Cu}}}\right\}$$

$$= \mathrm{Re}\left\{A_s\, e^{i\boldsymbol{Q}\cdot\boldsymbol{r_{Cu}}}\right\} \quad (1.10)$$

$$n(\boldsymbol{r_{O_x}}) = 2K'\mathrm{Re}\left\{[\textstyle\sum_k \cos(k_x)\, P(\boldsymbol{k},\boldsymbol{Q})]e^{i\boldsymbol{Q}\cdot\boldsymbol{r_{O_x}}}\right\}$$

$$= \mathrm{Re}\left\{[A_{s'} + A_d]e^{i\boldsymbol{Q}\cdot\boldsymbol{r_{O_x}}}\right\} \quad (1.11)$$

$$n(\boldsymbol{r_{O_y}}) = 2K'\mathrm{Re}\left\{\left[\textstyle\sum_k \cos\left(k_y\right) P(\boldsymbol{k},\boldsymbol{Q})\right]e^{i\boldsymbol{Q}\cdot\boldsymbol{r_{O_y}}}\right\}$$

$$= \mathrm{Re}\left\{[A_{s'} - A_d]e^{i\boldsymbol{Q}\cdot\boldsymbol{r_{O_y}}}\right\} \quad (1.12)$$

with $A_s = KP_s$ and $A_{s',d} = K'P_{s',d}$. Our Fourier transforms of the STM data in Fig. 3 of the main text yield the prefactors in Eqs. (1.11 & 1.12). The observed change in sign between the prefactors demonstrates that $|P_d| \gg |P_{s'}|$ as anticipated in Refs. [22, 23,24].

II Symmetry Decomposition of CuO_2 IUC States

Here we present mathematical details behind the angular momentum form factor organization of density waves on the CuO_2 plane. There are many ways of organizing density waves in the CuO_2 plane. One organization is to think of them as a wave on the copper atoms, a wave on the x-axis bond oxygen atoms and a wave on the y-axis bond oxygen atoms. Another organization is in terms of amplitudes of three different Bragg reflected peaks such as

$$n(\boldsymbol{r_n}) = A\cos \boldsymbol{q}\cdot\boldsymbol{r_n} + B\cos(\boldsymbol{q}+\boldsymbol{G_x})\cdot\boldsymbol{r_n} + C\cos\left(\boldsymbol{q}+\boldsymbol{G_y}\right)\cdot\boldsymbol{r_n} \quad (2.1)$$

where $\boldsymbol{r_n}$ is the location of either a copper or oxygen atom, $\boldsymbol{q}$ is the wave vector of the wave and $\boldsymbol{G_x} = (2\pi/a\,, 0)$, $\boldsymbol{G_y} = (0, 2\pi/a)$ are reciprocal lattice vectors. The amplitudes A, B and C here are related to the corresponding amplitudes of the same wave organized in terms of waves on the copper and two oxygen atoms within the unit cell through a simple linear relation. The results presented in the main manuscript, however, present a compelling case that a third organization captures the density wave observed near $\boldsymbol{q} = (2\pi/4a\,, 0)$ and $\boldsymbol{q} = (0, 2\pi/4a)$ in STM experiments performed on underdoped cuprate superconductors at the pseudogap energy scale *in a remarkably simple way*. This way organizes them by angular momentum form factors that we call s, s' ("extended s") and d. Organized this way, the observed density wave within experimental resolution has a finite amplitude for only its d-wave form factor.

We can think of the angular momentum form factor organization as a modulation of $\boldsymbol{q} = 0$ "waves" whose point group symmetry is well defined, as shown in Fig. 1A of the main text. The $\boldsymbol{q} = 0$ s-wave has a density

$$n(\boldsymbol{r_{Cu}}) = A_s\ n\left(\boldsymbol{r_{O_x}}\right) = 0\ n\left(\boldsymbol{r_{O_y}}\right) = 0 \quad (2.2)$$

, the $\boldsymbol{q} = 0$ s'-wave has density

$$n(\boldsymbol{r_{Cu}}) = 0,\ n\left(\boldsymbol{r_{O_x}}\right) = A_{s'}, n\left(\boldsymbol{r_{O_y}}\right) = A_{s'} \quad (2.3)$$

, and the $\boldsymbol{q} = 0$ d-wave has density

$$n(\boldsymbol{r_{Cu}}) = 0, n\left(\boldsymbol{r_{O_x}}\right) = A_d, n\left(\boldsymbol{r_{O_y}}\right) = -A_d \quad (2.4).$$

. Modulating these waves, we then obtain

$$n_s(\boldsymbol{r_n}) = \begin{cases} A_s\cos\boldsymbol{q}\cdot\boldsymbol{r_n}, & \boldsymbol{r_n} = \boldsymbol{r_{Cu}}, \\ 0, & \boldsymbol{r_n} = \boldsymbol{r_{O_x}}, \\ 0, & \boldsymbol{r_n} = \boldsymbol{r_{O_y}}, \end{cases} \qquad n_{s'}(\boldsymbol{r_n}) = \begin{cases} 0, & \boldsymbol{r_n} = \boldsymbol{r_{Cu}}, \\ A_{s'}\cos\boldsymbol{q}\cdot\boldsymbol{r_n}, & \boldsymbol{r_n} = \boldsymbol{r_{O_x}}, \\ A_{s'}\cos\boldsymbol{q}\cdot\boldsymbol{r_n}, & \boldsymbol{r_n} = \boldsymbol{r_{O_y}}, \end{cases}$$

$$n_d(\boldsymbol{r_n}) = \begin{cases} 0, & \boldsymbol{r_n} = \boldsymbol{r_{Cu}}, \\ A_d\cos\boldsymbol{q}\cdot\boldsymbol{r_n}, & \boldsymbol{r_n} = \boldsymbol{r_{O_x}}, \\ -A_d\cos\boldsymbol{q}\cdot\boldsymbol{r_n}, & \boldsymbol{r_n} = \boldsymbol{r_{O_y}}, \end{cases} \quad (2.5)$$

A graphical picture corresponding to these waves is presented in Fig. 2A,B,C of the main text.

Given these waves, we would like to understand how they relate to the other organizations discussed above. To understand the organization by Bragg reflected peaks we need merely Fourier transform. The result is presented in Figs. 1D,E,F of the main text. We then see that a density wave with the s-wave form factor has amplitudes A = A_s, B=A_s, C=A_s, an s'-wave form factor has amplitudes A = $A_{s'}$, B = C = 0 and a d-wave form factor has amplitudes A = 0, B = -C = A_d.

Consider also the organization by atomic site. We see that the s-wave form factor is just a wave purely on the copper atoms with no weight on the oxygen atoms while the s'-wave and d-wave form factors involve purely the oxygen sites. There is also a curious but practically very important relationship between the s'-wave and d-wave form factors: in a sense they are like mirror images of each other. Consider the s'-wave form factor. Organized by atomic site, we then consider the two functions

$$n_{Ox}(\boldsymbol{r_n}) = \begin{cases} 0, & \boldsymbol{r_n} = \boldsymbol{r_{Cu}}, \\ A_{s'}\cos \boldsymbol{q}\cdot\boldsymbol{r_n}, & \boldsymbol{r_n} = \boldsymbol{r_{O_x}}, \\ 0, & \boldsymbol{r_n} = \boldsymbol{r_{O_y}}, \end{cases} \quad n_{Oy}(\boldsymbol{r_n}) \begin{cases} 0, & \boldsymbol{r_n} = \boldsymbol{r_{Cu}}, \\ 0, & \boldsymbol{r_n} = \boldsymbol{r_{O_x}}, \\ A_{s'}\cos \boldsymbol{q}\cdot\boldsymbol{r_n}, & \boldsymbol{r_n} = \boldsymbol{r_{O_y}}, \end{cases} \quad (2.6)$$

with $n_{Cu}(\boldsymbol{r_n}) = 0$.

Anticipating the result of Section III, taking the sum $\tilde{n}_{Ox}(\boldsymbol{q}) + \tilde{n}_{Ox}(\boldsymbol{q})$ must recover the Fourier transform of the full s'-wave. However, taking the difference $\tilde{n}_{Ox}(\boldsymbol{q}) - \tilde{n}_{Oy}(\boldsymbol{q})$, we obtain the Fourier transform of the d-wave form factor. Similarly, $\tilde{n}_{Ox}(\boldsymbol{q}) + \tilde{n}_{Oy}(\boldsymbol{q})$ for a density wave with a pure d-wave form factor must recover the corresponding Fourier transform presented in Fig. 2I but the difference $\tilde{n}_{Ox}(\boldsymbol{q}) - \tilde{n}_{Ox}(\boldsymbol{q})$ will look like the Fourier transform of a density with a pure s'-wave form factor in Fig. 2H. In this way, we see that for pure d-wave or s'-wave form factor density waves, there is a striking difference between the sum and difference of the atomic site organization waves and that the different cases always looks like the Fourier transform of the other form factor.

Finally, given the above understanding of how the overall electronic structure image (e.g. R($\boldsymbol{r}$)) is built up from its components, there is another possible approach to determining the form factor of any density wave. Phase-resolved Fourier analysis of such an electronic structure image that has not been decomposed into its constituent parts Cu($\boldsymbol{r}$), O_x($\boldsymbol{r}$), O_y($\boldsymbol{r}$) but remains intact, should still reveal the relative magnitude of the three form factors. However, one can show that this is only possible if the three independent DW peaks at **Q**, **Q'** = (1,0) + **Q** and **Q''** = (0,1)+**Q**, are well resolved.

III Predicted Fourier Transform STM Signatures of a IUC Nematic DW

As discussed in SI sections I and II, the projection of a density wave (DW) into s, s' and d form factor components is conceptually appealing. However, for the purposes of this section we will keep in mind the exigencies of the experimental technique and work in terms of the segregated oxygen sub-lattice images $O_{x,y}(\boldsymbol{r})$. In terms of the segregated sub-lattices, a d-wave form factor DW is one for which the DW on the O_x sites is in anti-phase with that on the O_y sites. For $\mathbf{q}\neq 0$ ordering the form factor does not uniquely determine the point group symmetry of the DW and hence in general s, s' and d form factors are free to mix. This section predicts the consequences of a primarily d-wave form factor density wave for $\tilde{O}_{x,y}(\boldsymbol{q})$ and shows its consistency with the data presented in the main text.

To deduce the logical consequences a d-wave form factor DW for the Fourier transforms of the segregated oxygen site images one can start by constructing the dual real and momentum-space representation of the sub-lattices:

$$L_{Cu}(\boldsymbol{r}) = \sum_{i,j} \delta(\boldsymbol{r} - \boldsymbol{R_{i,j}}) \Leftrightarrow \tilde{L}_{Cu}(\boldsymbol{q}) = \sum_{h,k} \delta(\boldsymbol{q} - \boldsymbol{G^{h,k}}) \quad (3.1)$$

$$L_{O_x}(\vec{r}) = L_{Cu}\left(\boldsymbol{r} - \frac{a_0\hat{\boldsymbol{x}}}{2}\right) \Leftrightarrow \tilde{L}_{O_x}(\boldsymbol{q}) = e^{i\boldsymbol{q}\cdot\frac{a_0\hat{x}}{2}}\tilde{L}_{Cu}(\boldsymbol{q}) \quad (3.2)$$

$$L_{O_y}(\vec{r}) = L_{Cu}\left(\boldsymbol{r} - \frac{a_0\hat{\boldsymbol{y}}}{2}\right) \Leftrightarrow \tilde{L}_{O_y}(\boldsymbol{q}) = e^{i\boldsymbol{q}\cdot\frac{a_0\hat{y}}{2}}\tilde{L}_{Cu}(\boldsymbol{q}) \quad (3.3)$$

. The $\{\boldsymbol{R_{i,j}}\}$ are the set of direct lattice vectors of the square lattice with lattice constant a_0 and the $\{\boldsymbol{G^{h,k}}\}$ are the reciprocal lattice vectors. The displacement of the oxygen sub-lattices from the copper sub-lattice has the effect of modulating the phase of their Bragg peaks along the direction of displacement with periodicity $\frac{4\pi}{a_0}$ in reciprocal space. This is depicted in Fig. S1A.

Using the convolution theorem, a d-wave form factor modulation of the oxygen site density takes on the dual description:

$$O_x(\boldsymbol{r}) = L_{O_x}(\boldsymbol{r}) \cdot A_{O_x}(\boldsymbol{r}) \Leftrightarrow \tilde{O}_x(\boldsymbol{q}) = \tilde{L}_{O_x}(\boldsymbol{q}) * \tilde{A}_{O_x}(\boldsymbol{q}) \quad (3.4)$$

$$O_y(\boldsymbol{r}) = L_{O_y}(\boldsymbol{r}) \cdot A_{O_y}(\boldsymbol{r}) \Leftrightarrow \tilde{O}_y(\boldsymbol{q}) = \tilde{L}_{O_y}(\boldsymbol{q}) * \tilde{A}_{O_y}(\boldsymbol{q}) \quad (3.5)$$

$$A_{O_x}(\boldsymbol{r}) = -A_{O_y}(\boldsymbol{r}) = A(\boldsymbol{r}) \Leftrightarrow \tilde{A}_{O_x}(\boldsymbol{q}) = -\tilde{A}_{O_y}(\boldsymbol{q}) = A(\boldsymbol{q}) \quad (3.6)$$

. The functions $O_{x,y}(\boldsymbol{r})$ are the segregated oxygen sub-lattice images. The $A_{O_{x,y}}(\boldsymbol{r})$ are continuous functions that when multiplied by the sub-lattice functions yield density waves in anti-phase on the separate oxygen sub-lattices (Fig. S1B) . Fig. S1C shows their

Fourier transforms $\widetilde{\mathrm{A}}_{\mathrm{O_{x,y}}}(\boldsymbol{q})$. Note that $\mathrm{A}(\boldsymbol{r})$ may contain arbitrary amplitude and overall phase disorder and remain d-wave so long as the relative phase relation in Eq. (3.6) is maintained.

As shown in Fig. S2A, the convolutions in Eqs. (3.4) & (3.5) create an image of $\widetilde{\mathrm{A}}_{\mathrm{O_{x,y}}}(\boldsymbol{q})$ at each reciprocal lattice vector that sum to form the total convolution. Labelling the convolution image due to the reciprocal lattice vector (h,k) in the x sub-lattice $\widetilde{\mathrm{O}}_{\mathrm{x}}^{h,k}(\boldsymbol{q})$:

$$\widetilde{\mathrm{O}}_{\mathrm{x}}(\boldsymbol{q}) = \sum_{h,k} \widetilde{\mathrm{O}}_{\mathrm{x}}^{h,k}(\boldsymbol{q}) = \sum_{n} e^{i\boldsymbol{G^{h,k}}.\frac{a_0\hat{\boldsymbol{x}}}{2}} \widetilde{\mathrm{A}}_{\mathrm{O_x}}\left(\boldsymbol{q} - \boldsymbol{G^{h,k}}\right) \tag{3.7}$$

. In creating the (h,k) convolution image, the phase of the sub-lattice Bragg peak at $\vec{G}^{h,k}$ and that of the form factor $\widetilde{\mathrm{A}}_{\mathrm{O_x}}(\vec{q})$ must be added:

$$\arg\left\{\widetilde{\mathrm{O}}_{\mathrm{x}}^{h,k}(\boldsymbol{q})\right\} = \arg\{\widetilde{\mathrm{A}}_{\mathrm{O_x}}(\boldsymbol{q})\} + \arg\left\{e^{i\boldsymbol{G^{h,k}}.\frac{a_0\hat{\boldsymbol{x}}}{2}}\right\} \tag{3.8}$$

. Thus it follows immediatley that

$$\widetilde{\mathrm{O}}_{\mathrm{x}}^{0,0} = \mathrm{A}(\boldsymbol{q})\ \ \widetilde{\mathrm{O}}_{\mathrm{y}}^{0,0} = -\mathrm{A}(\boldsymbol{q}) \tag{3.9}$$

$$\widetilde{\mathrm{O}}_{\mathrm{x}}^{1,0} = -\mathrm{A}(\boldsymbol{q})\ \widetilde{\mathrm{O}}_{\mathrm{y}}^{1,0} = -\mathrm{A}(\boldsymbol{q}) \tag{3.10}$$

$$\widetilde{\mathrm{O}}_{\mathrm{x}}^{0,1} = \mathrm{A}(\boldsymbol{q})\quad \widetilde{\mathrm{O}}_{\mathrm{y}}^{0,1} = \mathrm{A}(\boldsymbol{q}) \tag{3.11}$$

and hence

$$\widetilde{\mathrm{O}}_{\mathrm{x}}^{0,0} + \widetilde{\mathrm{O}}_{\mathrm{y}}^{0,0} = 0 \qquad \widetilde{\mathrm{O}}_{\mathrm{x}}^{0,0} - \widetilde{\mathrm{O}}_{\mathrm{y}}^{0,0} = 2\mathrm{A}(\boldsymbol{q}) \tag{3.12}$$

$$\widetilde{\mathrm{O}}_{\mathrm{x}}^{1,0} + \widetilde{\mathrm{O}}_{\mathrm{y}}^{1,0} = -2\mathrm{A}(\boldsymbol{q}) \qquad \widetilde{\mathrm{O}}_{\mathrm{x}}^{1,0} - \widetilde{\mathrm{O}}_{\mathrm{y}}^{1,0} = 0 \tag{3.13}$$

$$\widetilde{\mathrm{O}}_{\mathrm{x}}^{0,1} + \widetilde{\mathrm{O}}_{\mathrm{y}}^{0,1} = 2\mathrm{A}(\boldsymbol{q}) \qquad \widetilde{\mathrm{O}}_{\mathrm{x}}^{0,1} - \widetilde{\mathrm{O}}_{\mathrm{y}}^{0,1} = 0 \tag{3.14}$$

A direct consequence of a d-wave form factor is that in $\widetilde{\mathrm{O}}_{\mathrm{x}}(\boldsymbol{q}) + \widetilde{\mathrm{O}}_{\mathrm{y}}(\boldsymbol{q})$ the amplitude of the convolution image at (0,0) is cancelled exactly whereas those at the (±1,0) and(0, ±1) points are enhanced as illustrated in Figs. S2B&C. The converse is true for $\widetilde{\mathrm{O}}_{\mathrm{x}}(\boldsymbol{q}) - \widetilde{\mathrm{O}}_{\mathrm{y}}(\boldsymbol{q})$. This holds for any d-wave modulation in the presence of arbitrary amplitude and overall phase disorder.

Figs. 2G-I of the main text show Fourier transforms of different form factor density waves in the CuO_2 plane; for pedagogical reasons we labeled them $\tilde{S}_{DW}(\boldsymbol{q})$, $\tilde{S'}_{DW}(\boldsymbol{q})$ and $\widetilde{D}_{DW}(\boldsymbol{q})$, with the obvious notation. A d-form factor density wave has modulations only on the oxygen sites and hence its contribution to the full Fourier transform is contained entirely within $\widetilde{\mathrm{O}}_{\mathrm{x}}(\boldsymbol{q}) + \widetilde{\mathrm{O}}_{\mathrm{y}}(\boldsymbol{q})$. From Eqs. (3.12-3.14) we must conclude that for density waves with principal wave-vectors that lie within the 1st BZ, $\widetilde{D}_{DW}(\boldsymbol{q})$ will exhibit an absence of peaks at these wave-vectors in the 1st BZ. For $\tilde{S}(\boldsymbol{q})$ and $\tilde{S}'(\boldsymbol{q})$ we may conclude that they will be present using similar arguments.

Empirically (main text Figs. 4 and 5), our data contain modulations at two wavevectors $\mathbf{Q_1}$=(Q_0,0) and $\mathbf{Q_2}$=(0,Q_0) with $Q_0 \approx 1/4$ but with a great deal of fluctuation in the spatial-phase of the DW (see Ref. 43 of main text). However, it would be improper to conclude from this that we observe a bi-directional d-wave DW, often termed the "checkerboard" modulation. The strong disorder of the density modulations in BSCCO and NaCCOC is apparent in the real-space images presented in Fig. 3 of the main text and Section V of this document. Random charge disorder can have the effect of taking a clean system with an instability toward uni-directional ("stripe") ordering and produce domains of uni-directional order than align with the local anisotropy. Conversely, a clean system with an instability towards bi-directional ("checkerboard") ordering may have local anisotropy imbued upon it by disorder.

Whilst the wave-vector(s) of the underlying instability of the copper oxide plane to DW ordering are of keen theoretical interest, pragmatically, any d-wave form factor DW containing two wave-vectors can be described by:

$$\mathrm{A}(\boldsymbol{r}) = \cos(\boldsymbol{Q_1} \cdot \boldsymbol{r}\ ) \cdot \mathrm{H}_1(\boldsymbol{r}) + \cos(\boldsymbol{Q_2} \cdot \boldsymbol{r}\ ) \cdot \mathrm{H}_2(\boldsymbol{r}) \tag{3.15}$$

$$\mathrm{A}(\boldsymbol{q}) = \tfrac{1}{2}[\delta(\boldsymbol{q} - \boldsymbol{Q_1}) + \delta(\boldsymbol{q} + \boldsymbol{Q_1}\ )] * \widetilde{\mathrm{H}}_1(\boldsymbol{q}) + \tfrac{1}{2}[\delta(\boldsymbol{q} - \boldsymbol{Q_2}) + \delta(\boldsymbol{q} + \boldsymbol{Q_2}\ )] * \widetilde{\mathrm{H}}_2(\boldsymbol{q}) \tag{3.16}$$

. The complex valued functions $\mathrm{H}_{x,y}(\boldsymbol{r})$ locally modulate the amplitude and phase of the density wave and hence encode its disorder. The problem now reduces to performing the convolutions contained in Eqs. (3.4,3.5&3.6).

For the specific example of $\vec{Q}_1 \approx (\frac{1}{4}, 0)$ and $\vec{Q}_2 \approx \left(0, \frac{1}{4}\right)$ considered in our study the primarily d-wave form factor requires that the peaks at $(\pm\frac{1}{4}, 0)$ and $\left(0, \pm\frac{1}{4}\right)$ present in both $\widetilde{\mathrm{O}}_x(\boldsymbol{q})$ and $\widetilde{\mathrm{O}}_y(\boldsymbol{q})$ must cancel exactly in $\widetilde{\mathrm{O}}_x(\boldsymbol{q}) + \widetilde{\mathrm{O}}_y(\boldsymbol{q})$ and be enhanced in $\widetilde{\mathrm{O}}_x(\boldsymbol{q}) - \widetilde{\mathrm{O}}_y(\boldsymbol{q})$. Conversely the peaks at $(\pm 1 \pm \frac{1}{4}, \pm 1 \pm \frac{1}{4})$ will be enhanced in $\widetilde{\mathrm{O}}_x(\boldsymbol{q}) + \widetilde{\mathrm{O}}_y(\boldsymbol{q})$ but will cancel exactly in $\widetilde{\mathrm{O}}_x(\boldsymbol{q}) - \widetilde{\mathrm{O}}_y(\boldsymbol{q})$. These are necessary consequences of a DW with a primarily *d*-wave form factor. This is discussed in the main text and in accord with the observations in Figs. 3& 4.

IV Sublattice Phase Definition: Lawler-Fujita Algorithm

Consider an atomically resolved STM topograph ,$T(\boldsymbol{r})$, with tetragonal symmetry where two orthogonal wavevectors generate the atomic corrugations.These are centered at the first reciprocal unit cell Bragg wavevectors $\boldsymbol{Q}_a = (Q_{ax}, Q_{ay})$ and $\boldsymbol{Q}_b = (Q_{bx}, Q_{by})$ with $\boldsymbol{a}$ and $\boldsymbol{b}$ being the unit cell vectors. Schematically, the ideal topographic image can be written as

$$T(\boldsymbol{r}) = T_0[\cos(\boldsymbol{Q}_a \cdot \boldsymbol{r}) + \cos(\boldsymbol{Q}_b \cdot \boldsymbol{r})] \quad (4.1)$$

. In SI-STM, the $T(\boldsymbol{r})$ and its simultaneously measured spectroscopic current map, $I(\boldsymbol{r}, V)$, and differential conductance map, $g(\boldsymbol{r}, V)$, are specified by measurements on a square array of pixels with coordinates labeled $\boldsymbol{r} = (x, y)$. The power-spectral-density (PSD) Fourier transform of $T(\boldsymbol{r})$, $\left|\tilde{T}(\boldsymbol{q})\right|^2$-where $\tilde{T}(\boldsymbol{q}) = Re\,\tilde{T}(\boldsymbol{q}) + iIm\,\tilde{T}(\boldsymbol{q})$, then exhibits two distinct peaks at $\boldsymbol{q} = \boldsymbol{Q}_a$and $\boldsymbol{Q}_b$.

In an actual experiment, $T(\boldsymbol{r})$ suffers picometer scale disortions from the ideal representation in (4.1) according to a slowly varying 'displacement field', $\boldsymbol{u}(\boldsymbol{r})$. The same distortion is also found in the spectroscopic data. Thus, a topographic image, including distortions, is schematically written as

$$T(\boldsymbol{r}) = T_0\left[\cos\left(\boldsymbol{Q}_a \cdot (\boldsymbol{r}+\boldsymbol{u}(\boldsymbol{r}))\right) + \cos\left(\boldsymbol{Q}_b \cdot (\boldsymbol{r}+\boldsymbol{u}(\boldsymbol{r}))\right)\right]. \quad (4.2)$$

Then, to remove the effects of $\boldsymbol{u}(\boldsymbol{r})$ requires an affine transformation at each point in space.

To begin, define the local phase of the atomic cosine components, at a given point $\boldsymbol{r}$, as

$$\begin{aligned} \varphi_a(\boldsymbol{r}) &= \boldsymbol{Q}_a \cdot \boldsymbol{r} + \theta_a(\boldsymbol{r}) \\ \varphi_b(\boldsymbol{r}) &= \boldsymbol{Q}_b \cdot \boldsymbol{r} + \theta_b(\boldsymbol{r}) \end{aligned} \quad (4.3)$$

which recasts equation (4.2) as

$$T(\boldsymbol{r}) = T_0\left[\cos\left(\varphi_a(\boldsymbol{r})\right) + \cos\left(\varphi_b(\boldsymbol{r})\right)\right] \quad (4.4)$$

where $\theta_i(\boldsymbol{r}) = \boldsymbol{Q}_i \cdot \boldsymbol{u}(\boldsymbol{r})$ is additional phase generated by the displacement field. If there were no distortions and the $T(\boldsymbol{r})$ image were perfectly periodic then $\theta_i(\boldsymbol{r})$ would be constant. From this perspective, the 2-dimensional lattice in (4.4) is a function of phase alone. For example, the apex of every atom in the topographic image has the same phase, $0(\mathrm{mod}\ 2\pi)$ regardless of where it is in the image. When viewed in the $\boldsymbol{r}$ coordinates, the distance between such points of equal phase in the 'perfect' lattice and distorted lattice is not the same. The problem of correcting $T(\boldsymbol{r})$ then reduces to finding a transformation to map the distorted lattice onto the 'perfect' one, using the phase information $\varphi_i(\boldsymbol{r})$. This is equivalent to finding a set of local transformations which makes $\theta_a(\boldsymbol{r})$ and $\theta_b(\boldsymbol{r})$ constant over all space; call them $\bar{\theta}_a$ and $\bar{\theta}_b$ respectively.

Let $\boldsymbol{r}$ be a point on the unprocessed $T(\boldsymbol{r})$ and let $\tilde{\boldsymbol{r}}$ be the point of equal phase on the perfect lattice periodic image, which needs to be determined. This produces a set of equivalency relations

$$\boldsymbol{Q}_a \cdot \boldsymbol{r} + \theta_a(\boldsymbol{r}) = \boldsymbol{Q}_a \cdot \tilde{\boldsymbol{r}} + \bar{\theta}_a$$

$$\boldsymbol{Q}_b \cdot \boldsymbol{r} + \theta_b(\boldsymbol{r}) = \boldsymbol{Q}_b \cdot \tilde{\boldsymbol{r}} + \bar{\theta}_b \tag{4.5}$$

Solving for $\tilde{\boldsymbol{r}} = (\tilde{x}, \tilde{y})$ and then assigning the values of the topographic image at $\boldsymbol{r} = (x, y)$, $T(\boldsymbol{r})$, to $\tilde{\boldsymbol{r}}$ produces the 'perfect' lattice. To solve for $\tilde{\boldsymbol{r}}$ rewrite (4.5) in matrix form

$$\boldsymbol{Q}\begin{pmatrix}\tilde{x}\\ \tilde{y}\end{pmatrix} = \boldsymbol{Q}\begin{pmatrix}x\\ y\end{pmatrix} - \begin{pmatrix}\bar{\theta}_a - \theta_a(\boldsymbol{r})\\ \bar{\theta}_a - \theta_b(\boldsymbol{r})\end{pmatrix} \tag{4.6}$$

where

$$\boldsymbol{Q} = \begin{pmatrix}Q_{ax} & Q_{ay}\\ Q_{bx} & Q_{by}\end{pmatrix}. \tag{4.7}$$

Because $\boldsymbol{Q}_a$ and $\boldsymbol{Q}_b$ are orthogonal, $\boldsymbol{Q}$ is invertible allowing one to solve for the displacement field $\boldsymbol{u}(\boldsymbol{r})$ which maps $\boldsymbol{r}$ to $\tilde{\boldsymbol{r}}$:

$$\boldsymbol{u}(\boldsymbol{r}) = \boldsymbol{Q}^{-1}\begin{pmatrix}\bar{\theta}_a - \theta_a(\boldsymbol{r})\\ \bar{\theta}_b - \theta_b(\boldsymbol{r})\end{pmatrix}. \tag{4.8}$$

In practice, we use the convention $\bar{\theta}_i = 0$ which generates a 'perfect' lattice with an atomic peak centered at the origin. This is equivalent to setting to zero the imaginary component of the Bragg peaks in the Fourier transform.

Of course, to employ the transformation in (4.6) one must first extract $\theta_i(\boldsymbol{r})$ from the topographic data. This is accomplished by using a computational lock-in technique in which the topograph, $T(\boldsymbol{r})$, is multiplied by reference sine and cosine functions with periodicity set by $\boldsymbol{Q}_a$and $\boldsymbol{Q}_b$. The resulting four images are filtered to retain only the $\boldsymbol{q}$-space regions within a radius $\delta q = \frac{1}{\lambda}$ of the four Bragg peaks; the magnitude of λ is chosen to capture only the relevant image distortions. This procedure results in retaining the local phase information $\theta_a(\boldsymbol{r}), \theta_b(\boldsymbol{r})$ that quantifies the local displacements from perfect periodicity:

$$Y_i(\boldsymbol{r}) = \sin\theta_i(\boldsymbol{r}), \quad X_i(\boldsymbol{r}) = \cos\theta_i(\boldsymbol{r}) \tag{4.9}$$

Dividing the appropriate pair of images allows one to extract $\theta_i(\boldsymbol{r})$:

$$\theta_i(\boldsymbol{r}) = \tan^{-1}\frac{Y_i(\boldsymbol{r})}{X_i(\boldsymbol{r})}. \tag{4.10}$$

V Data Analysis

In Fig. 5F of main text, we show the 2D histogram of the amplitude difference and the phase difference between $O_x(\mathbf{r})$ and $O_y(\mathbf{r})$. In order to construct this, first, "fouirer filter" is applied to get both real and imaginary part of $O_x(\mathbf{r})$ and $O_y(\mathbf{r})$ only associated with $\mathbf{Q}_x$~(1/4,0) and $\mathbf{Q}_y$~(0,1/4),

$$\tilde{O}_\alpha(\mathbf{r},\mathbf{Q}_\beta) = \int d\mathbf{R} O_\alpha(\mathbf{R})\, e^{i\mathbf{Q}_\beta\cdot\mathbf{R}} e^{-\frac{|\mathbf{r}-\mathbf{R}|^2}{2\Lambda^2}} \frac{1}{2\pi\Lambda^2}, \tag{5.1a}$$

where α, β=x, y, and Λ the averaging length to be ~30Å.
For $\mathbf{q}=\mathbf{Q}_x$, amplitudes and phases are given by

$$A_x(\mathbf{r},\mathbf{Q}_x) = \sqrt{Re\tilde{O}_x(\mathbf{r},\mathbf{Q}_x)^2 + Im\tilde{O}_x(\mathbf{r},\mathbf{Q}_x)^2}, \tag{5.1a}$$

$$A_y(\mathbf{r},\mathbf{Q}_x) = \sqrt{Re\tilde{O}_y(\mathbf{r},\mathbf{Q}_x)^2 + Im\tilde{O}_y(\mathbf{r},\mathbf{Q}_x)^2}, \tag{5.1b}$$

$$\phi_x(\mathbf{r},\mathbf{Q}_x) = tan^{-1}\left(\frac{Im\tilde{O}_x(\mathbf{r},\mathbf{Q}_x)}{Re\tilde{O}_x(\mathbf{r},\mathbf{Q}_x)}\right), \tag{5.2a}$$

$$\phi_y(\mathbf{r},\mathbf{Q}_x) = tan^{-1}\left(\frac{Im\tilde{O}_y(\mathbf{r},\mathbf{Q}_x)}{Re\tilde{O}_y(\mathbf{r},\mathbf{Q}_x)}\right). \tag{5.2b}$$

Similarly, for $\mathbf{q}=\mathbf{Q}_y$,

$$A_x(\mathbf{r},\mathbf{Q}_y) = \sqrt{Re\tilde{O}_x(\mathbf{r},\mathbf{Q}_y)^2 + Im\tilde{O}_x(\mathbf{r},\mathbf{Q}_y)^2}, \tag{5.3a}$$

$$A_y(\mathbf{r},\mathbf{Q}_y) = \sqrt{Re\tilde{O}_y(\mathbf{r},\mathbf{Q}_y)^2 + Im\tilde{O}_y(\mathbf{r},\mathbf{Q}_y)^2}, \tag{5.3b}$$

$$\phi_x(\mathbf{r},\mathbf{Q}_y) = tan^{-1}\left(\frac{Im\tilde{O}_x(\mathbf{r},\mathbf{Q}_y)}{Re\tilde{O}_x(\mathbf{r},\mathbf{Q}_y)}\right), \tag{5.4a}$$

$$\phi_y(\mathbf{r},\mathbf{Q}_y) = tan^{-1}\left(\frac{Im\tilde{O}_y(\mathbf{r},\mathbf{Q}_y)}{Re\tilde{O}_y(\mathbf{r},\mathbf{Q}_y)}\right). \tag{5.4b}$$

Next, the normalized amplitude difference and the phase difference for $\mathbf{q}=\mathbf{Q}_x$ are then defined by

$$\frac{A_x(\mathbf{r},\mathbf{Q}_x)-A_y(\mathbf{r},\mathbf{Q}_x)}{A_x(\mathbf{r},\mathbf{Q}_x)+A_y(\mathbf{r},\mathbf{Q}_x)}, \tag{5.5a}$$

$$|\phi_x(\mathbf{r},\mathbf{Q}_x) - \phi_y(\mathbf{r},\mathbf{Q}_x)| \tag{5.5b}$$

, respectively. Similarly, for $\mathbf{q}=\mathbf{Q}_y$,

$$\frac{A_x(\mathbf{r},\mathbf{Q}_y)-A_y(\mathbf{r},\mathbf{Q}_y)}{A_x(\mathbf{r},\mathbf{Q}_y)+A_y(\mathbf{r},\mathbf{Q}_y)}, \tag{5.6a}$$

$$|\phi_x(\mathbf{r},\mathbf{Q}_y) - \phi_y(\mathbf{r},\mathbf{Q}_y)|. \tag{5.6b}$$

Finally, using (5.5) and (5.6) we obtain a two dimensional histogram for both $\mathbf{Q}_x$ and $\mathbf{Q}_y$, independently, and then take sum of them to construct single distribution containing the information for both $\mathbf{Q}_x$ and $\mathbf{Q}_y$.

In Fig. S3 we show the measured $R(\boldsymbol{r})$ (subset of main Fig. 3A is presented since original FOV is so large DW is no longer visible clearly) and its segregation into three site-

specific images $C_u(\boldsymbol{r})$, $O_x(\boldsymbol{r})$ and $O_y(\boldsymbol{r})$ as described in the main text. With the origin set at a Cu site, Fig. S4 then shows the three complex valued Fourier transform images derived from Fig. 3A: $\tilde{C}_u(\boldsymbol{q}) \equiv Re\,\tilde{C}_u(\boldsymbol{q}) + iIm\,\tilde{C}_u(\boldsymbol{q})$, $\tilde{O}_x(\boldsymbol{q}) \equiv Re\tilde{O}_x(\boldsymbol{q}) + iIm\tilde{O}_x(\boldsymbol{q})$, $\tilde{O}_y(\boldsymbol{q}) \equiv Re\tilde{O}_y(\boldsymbol{q}) + iIm\tilde{O}_y(\boldsymbol{q})$. This type of sublattice-phase-resolved Fourier analysis which we introduce in this paper provides the capability to measure the relative phase of different sites with each CuO_2 unit cell. The inset to Fig. S3A shows the difference between the real component of Bragg intensity for (1,0) and (0,1) peaks in the Fourier transforms of the electronic structure images *before* sublattice segregation. It is this difference that was originally used to determine the *d*-form factor of the intra-unit-cell nematic state; see Ref. 12, 45 of main text. Figures S5 and S6 present the equivalent data and analysis for NaCCOC.

Figure S7 shows the comparison between the analysis of Z($\boldsymbol{r}$,|E|)=g($\boldsymbol{r}$,E)/g($\boldsymbol{r}$,-E) E=150meV for both BSCCO in S7A-D and NaCCOC in S7E-H. Both Z($\boldsymbol{r}$,|E|) are segregated into three site-specific images $C_u(\boldsymbol{r})$, $O_x(\boldsymbol{r})$ and $O_y(\boldsymbol{r})$. The analysis is then presented in terms of their complex Fourier transforms $Re\tilde{O}_x(\boldsymbol{q})$, $Re\tilde{O}_y(\boldsymbol{q})$ as described in the main text . One can see directly that the phenomena are extremely similar for both compounds , in terms of $Re\tilde{O}_x(\boldsymbol{q})$, $Re\tilde{O}_y(\boldsymbol{q})$ and $Re\tilde{O}_x(\boldsymbol{q})\pm Re\tilde{O}_y(\boldsymbol{q})$. Moreover they are in excellent agreement with expectations for a IUCN-DW in Fig 2H,I of main text . Thus, in the main text, we present analysis of Z($\boldsymbol{r}$,E=150) on an equivalent basis to R($\boldsymbol{r}$,E=150) when deriving $\tilde{O}_x(\boldsymbol{q}) \equiv Re\tilde{O}_x(\boldsymbol{q}) + iIm\tilde{O}_x(\boldsymbol{q})$, $\tilde{O}_y(\boldsymbol{q}) \equiv Re\tilde{O}_y(\boldsymbol{q}) + iIm\tilde{O}_y(\boldsymbol{q})$ for Fig. 3E-H of the main text.

References

[1] Nayak C (2000) Density –wave states of nonzero angular momentum. *Phys. Rev. B* 62(8): 4880-4889.

[2] Affleck I, Marston JB (1988) Large-n limit of the Heisenberg-Hubbard model: Implications for high-T_c superconductors. *Phys. Rev. B* 37(7): 3774-3777.

[3] Wang Z, Kotliar G, Wang X-F (1990) Flux-density wave and superconducting instability of the staggered-flux phase. *Phys. Rev. B* 42(13): 8690-8693.

[4] Chakravarty S, Laughlin RB, Morr DK, Nayak C (2001) Hidden order in the cuprates. *Phys. Rev. B* 63(9):094503-1—094503-10.

[5] Lee PA, Nagaosa N, Wen X-G (2006) Doping a Mott insulator: Physics of high-temperature superconductivity. *Rev. Mod. Phys*. 78(17):17-85.

[6] Laughlin RB (2014) Hartree-Fock computation of the high-T_c cuprate phase diagram. *Phys. Rev. B* 89(3):035134-1—035134-19 .

[7] Simon M E, Varma, CM (2002) Detection and Implications of a Time-Reversal Breaking State in Underdoped Cuprates. *Phys. Rev. Lett.* 89(24): 247003-1—247003-4.

[8] Kivelson SA, Fradkin E, Emery VJ (1998) Electronic liquid-crystal phases of a doped Mott insulator *Nature* 393: 550-553.

[9] Yamase H, Kohno H (2002) Instability toward Formation of Quasi-One-Dimensional Fermi Surface in Two-Dimensional t-J Model. *J. Phys. Soc. Jpn.* 69:2151-2157.

[10] Halboth CJ, Metzner W (2000) d-Wave Superconductivity and Pomeranchuk Instability in the Two-Dimensional Hubbard Model. *Phys. Rev. Lett.* 85(24):5162-5165.

[11] Sachdev S, Read N (1991) Large N expansion for frustrated and doped quantum antiferromagnets. *Int J Mod Phys B* 5(1):219-249.

[12] Vojta M, Sachdev S (1999) Charge Order, Superconductivity, and a Global Phase Diagram of Doped Antiferromagnets. *Phys. Rev. Lett.* 83(19):3916-3919.

[13] Vojta M, Zhang Y, Sachdev S (2000) Competing orders and quantum criticality in doped antiferromagnets. *Phys. Rev. B* 62(10): 6721-6744.

[14] M. Vojta (2002) Superconducting charge-ordered states in cuprates. *Phys. Rev. B* 66(10):104505-1—104505-5.

[15] Sachdev S (2003) Order and quantum phase transitions in the cuprate superconductors. *Rev. Mod. Phys.* 75(3):913-932.

[16] Vojta M, Rösch O (2008) Superconducting d-wave stripes in cuprates: Valence bond order coexisting with nodal quasiparticles. *Phys. Rev. B* 77(9):094504-1—094504-8 .

[17] Li J-X, Wu C-Q, Lee D-H (2006) Checkerboard charge density wave and pseudogap of high-T_c cuprate. *Phys. Rev. B* 74(18):184515-1—184515-6 (2006).

[18] Davis JC, Lee D-H (2013) Concepts relating magnetic interactions, intertwined electronic orders, and strongly correlated superconductivity. *Proc Nat Acad Sci* 110(44)**:**17623—17630.

[19] Seo K, Chen H-D, Hu J (2007) d-wave checkerboard order in cuprates. *Phys. Rev. B* 76(2):020511-1—020511-4.

[20] Newns DM, Tsuei CC (2007) Fluctuating Cu-O-Cu bond model of high-temperature superconductivity. *Nat Phys* 3(3):184-191.

[21] Metlitski MA, Sachdev S (2010) Quantum phase transitions of metals in two spatial dimensions. II. Spin density wave order. *Phys. Rev. B* 82(7):075128-1—075128-30.

[22] Sachdev S, La Placa R (2013) Bond order in two-dimensional metals with antiferromagnetic exchange interactions. *Phys Rev Lett* 111(2):027202-1—027202-5.

[23] Allais A, Bauer J, Sachdev S (2014) Bond order instabilities in a correlated two-dimensional metal. arXiv:1402.4807.
[24] Allais A, Bauer J, Sachdev S (2014) Auxiliary-boson and DMFT studies of bond ordering instabilities of t-J-V models on the square lattice. arXiv:1402.6311.
[25] Holder T, Metzner W (2012) Incommensurate nematic fluctuations in two-dimensional metals. *Phys. Rev. B* 85(16):165130-1—165130-7 (2012);
[26] Husemann C, Metzner W (2012) Incommensurate nematic fluctuations in the two-dimensional Hubbard model. *Phys. Rev. B* 86(8):085113-1— 085113-7.
[27] Bejas M, Greco A, Yamase H (2012) Possible charge instabilities in two-dimensional doped Mott insulators. *Phys. Rev. B* 86(22):224509-1—224509-12.
[28] Efetov KB, Meier H, Pépin C (2013) Pseudogap state near a quantum critical point. *Nat Phys* 9(7):442—446.
[29] Kee H-Y, Puetter CM, Stroud D (2013) Transport signatures of electronic-nematic stripe phases. *J. Phys. Condens. Matter* 25:202201-1—202201-6.
[30] Bulut S, Atkinson WA, Kampf AP (2013) Spatially modulated electronic nematicity in the three-band model of cuprate superconductors. *Phys Rev B* 88(15):155132-1—155132-13.
[31] Sau JD, Sachdev S (2014) Mean-field theory of competing orders in metals with antiferromagnetic exchange interactions. *Phys. Rev. B* 89(7):075129-1—075129-11 (2014).
[32] Meier H, Pépin C, Einenkel M, Efetov KB (2013) Cascade of phase transitions in the vicinity of a quantum critical point. arXiv:1312.2010.
[33] Wang Y, Chubukov AV (2014) Charge order and loop currents in hole-doped cuprates. arXiv:1401.0712.

Supporting Figure Captions

Figure S1 Sub-lattice Decomposition of d Form Factor DW

A. Fourier transforms of the x-bond and y-bond oxygen sublattices without a DW modulation.

B. Schematic of continuous functions $A_{O_{x,y}}(\boldsymbol{r})$ which when multiplied by the sublattice functions $L_{O_{x,y}}(\boldsymbol{r})$ yield density waves in anti-phase on the two sublattices with a modulation along the x direction.

C. Fourier transforms of the functions $A_{O_{x,y}}(\boldsymbol{r})$ exhibiting a relative phase of π as required for a d form factor density wave.

Figure S2 Fourier Analysis of DW using the Convolution Theorem

A. Schematic of the segrated sublattice images $O_{x,y}(\boldsymbol{r})$ and their Fourier transforms $\widetilde{O}_{x,y}(\boldsymbol{q})$ which can be obtained from Fig. S1 by application of the convolution theorem.

B. Sum and difference of $Re\widetilde{O}_x(\boldsymbol{q})$ and $Re\widetilde{O}_y(\boldsymbol{q})$ for a *d*-form factor density wave with modulation along the x direction at $\boldsymbol{Q}=(Q,0)$. Note that the origin of co-ordinates in real space has been chosen such that the Fourier transforms are purely real.

C. Sum and difference of $Re\widetilde{O}_x(\boldsymbol{q})$ and $Re\widetilde{O}_y(\boldsymbol{q})$ for a d form factor density wave with modulations along the x and y directions at $\boldsymbol{Q}=(Q,0),(0,Q)$. The key signature of the d-form factor is the absence of the peaks at $(Q,0),(0,Q)$ in $Re\widetilde{O}_x(\boldsymbol{q}) + Re\widetilde{O}_y(\boldsymbol{q})$ and their presence in $Re\widetilde{O}_x(\boldsymbol{q}) - Re\widetilde{O}_y(\boldsymbol{q})$; the converse being true for the DW peaks surrounding (±1, ±1).

Figure S3 Sublattice Segregation for BSCCO

A. Measured $R(\boldsymbol{r})$ for BSCCO sample with p~8±1%. This data is a subset of Fig. 3A reproduced here for clarity. The inset demonstrates an inequivalence between the real component of Bragg intensity for (1,0) and (0,1) peaks in the Fourier transforms of the electronic structure image *before* sublattice segregation signalling a Q=0 nematic state.

B. Copper site segregated image, $Cu(\boldsymbol{r})$, in which the spatial average is subracted, with copper sites selected from A.

C. x-bond oxygen segregated specific image, $O_x(\boldsymbol{r})$, in which the spatial average is subracted, with x-oxygen sites selected from A.

D. y-bond oxygen segregated specific image, $O_y(\boldsymbol{r})$, in which the spatial average is subracted, with y-oxygen sites selected from A.

Figure S4 Sublattice Phase Resolved Fourier Analysis for BSCCO

A. Measured $Re\mathrm{Cu}(\mathbf{q})$ for BSCCO sample in Fig. 3A. No DW peaks are discernable at $\boldsymbol{Q}=(Q,0),(0,Q)$ or as Bragg satellites surrounding(±1,0) and (0, ±1) . This indicates a very small s wave component for the density wave form factor.

B. Measured $Im\mathrm{Cu}(\mathbf{q})$ which also indicates a very small s wave component.

C. Measured $Re\mathrm{O_x}(\mathbf{q})$ showing DW peaks at $\boldsymbol{Q}=(Q,0),(0,Q)$ and corresponding Bragg satellites.

D. Measured $Im\mathrm{O_x}(\mathbf{q})$ which exhibits the same structure as C. The strong overall phase disorder is apparent in the colour variation within the DW peaks.

E. Measured $Re\mathrm{O_y}(\mathbf{q})$ which also shows DW peaks at $\boldsymbol{Q}=(Q,0),(0,Q)$ along with Bragg satellites.

F. Measured $Im O_y(\mathbf{q})$ which exhibits the same structure as E.

Figure S5 Sub-Lattice Segregation for NaCCOC

A. Measured $Z(\boldsymbol{r}, E=150mV)$ for NaCCOC sample with p~12±1%;. The inset demonstrates an inequivalence between the real component of Bragg intensity for (1,0) and (0,1) peaks in the Fourier transforms of the electronic structure image *before* sublattice segregation signalling a Q=0 nematic state, as Fig S3A

B. Copper site segregated image, $Cu(\boldsymbol{r})$, in which spatial average is subracted, with copper sites selected from A.

C. x-bond oxygen site segregared image, $O_x(\boldsymbol{r})$, in which the spatial average is subracted, with x-oxygen sites selected from A.

D. y-bond oxygen site segregated image, $O_y(\boldsymbol{r})$, in which the spatial average is subracted, with y-oxygen sites selected from A.

Figure S6 Sublattice Phase Resolved Fourier Analysis for NaCCOC

A. Measured $Re Cu(\mathbf{q})$ for NaCCOC sample with p~12±1%. No DW peaks are discernable at $\boldsymbol{Q}=(Q,0),(0,Q)$ or as Bragg satellites surrounding (±1,0) and (0, ±1). This indicates that the DW in NaCCOC has, like BSCCO, a very small s wave component in its form factor.

B. Measured $Im Cu(\mathbf{q})$.

C. Measured $Re O_x(\mathbf{q})$ showing DW peaks at $\boldsymbol{Q}=(Q,0),(0,Q)$ and corresponding Bragg satellites.

D. Measured $Im O_x(\mathbf{q})$ which exhibits the same structure as C. The colour variation within the DW peaks is smaller for NaCCOC than for BSCCO indicating a less disordered DW.

E. Measured $Re O_y(\mathbf{q})$ which also shows DW peaks at $\boldsymbol{Q}=(Q,0),(0,Q)$ along with Bragg satellites.

F. Measured $Im O_y(\mathbf{q})$ which exhibits the same structure as E.

Figure S7 Comparison of Z(r,E=150meV) between BSCCO and NaCCOC

A. Measured $O_x(\boldsymbol{q})$ for BSCCO sample with p~8±1% obtained using Z(***r***,|E|)=g(***r***,E)/g(***r***,-E), E=150meV.

B. Measured $O_y(\boldsymbol{q})$ for BSCCO sample using same analysis as in A.

C. Measured $Re\tilde{O}_x(\boldsymbol{q}) + Re\tilde{O}_y(\boldsymbol{q})$ from A,B. The absence of the four DW peaks at $\boldsymbol{Q}$ is characteristic of a d form factor DW.

D. Measured $Re\tilde{O}_x(\boldsymbol{q}) - Re\tilde{O}_y(\boldsymbol{q})$ from A,B. The presence of the four DW peaks at $\boldsymbol{Q}$ and absence of the Bragg satellite peaks is another expectation for a d form factor DW.

E. Measured $O_x(\boldsymbol{q})$ for NaCCOC sample with p~12±+-1% obtained using Z(***r***,|E|)=g(***r***,E)/g(***r***,-E), E=150meV.

F. Measured $O_y(\boldsymbol{q})$ for NaCCOC sample using same analysis as in E.

G. Measured $Re\tilde{O}_x(\boldsymbol{q}) + Re\tilde{O}_y(\boldsymbol{q})$ from E,F. The same key signature of a d form factor DW is present in this measurement of NaCCOC as is present in that for BSCCO in C.

H. Measured $Re\tilde{O}_x(\boldsymbol{q}) - Re\tilde{O}_y(\boldsymbol{q})$ from E,F. The signatures of a d form factor DW are once again seen for NaCCOC in this image and should be compared to that for BSCCO in D.

S1

A

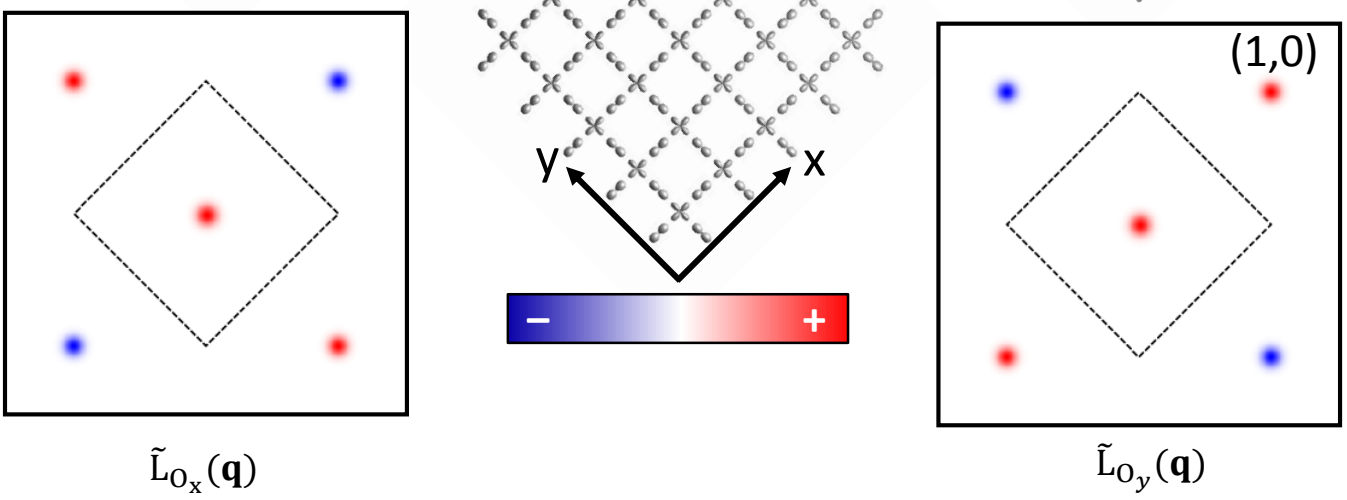

$\tilde{L}_{O_x}(\mathbf{q})$ $\tilde{L}_{O_y}(\mathbf{q})$

B

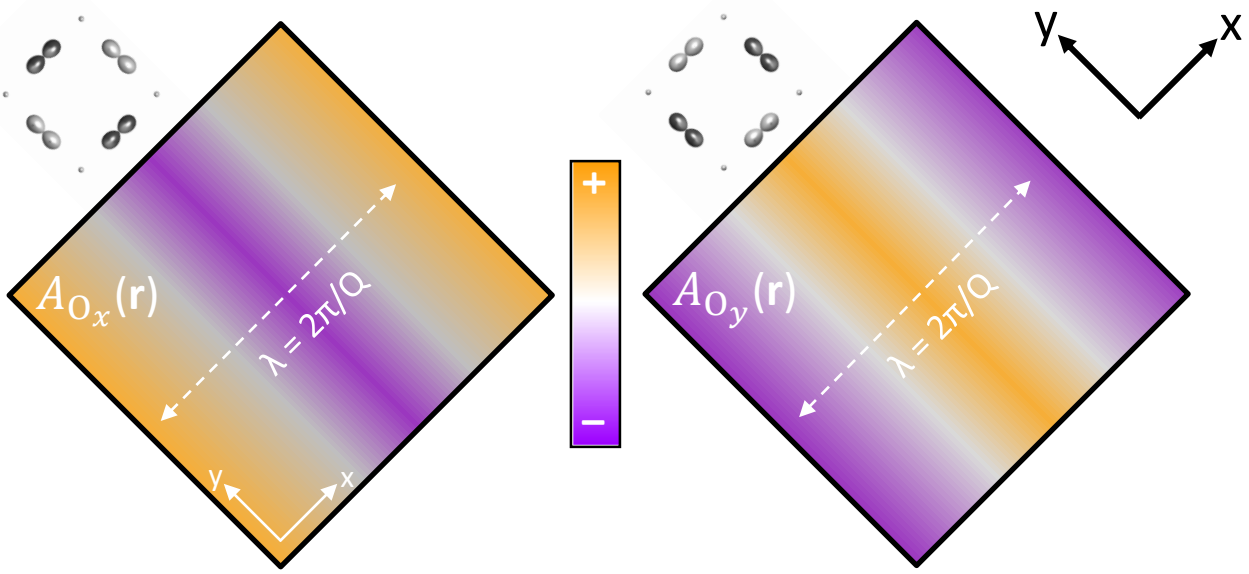

C

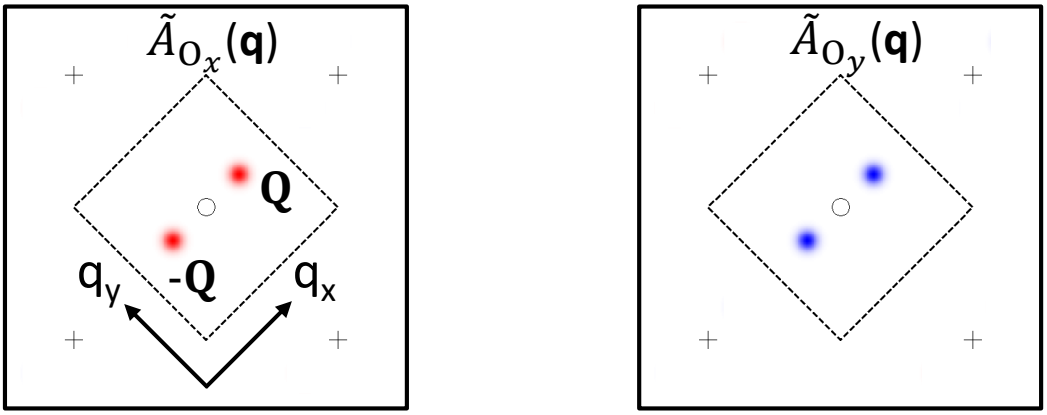

S2

A

$O_x(\mathbf{r})$

+

−

$O_y(\mathbf{r})$

$\tilde{O}_x(\mathbf{q}) = \tilde{A}_{O_x}(\mathbf{q}) * \tilde{L}_{O_x}(\mathbf{q})$

q_y q_x

$\tilde{O}_y(\mathbf{q}) = \tilde{A}_{O_y}(\mathbf{q}) * \tilde{L}_{O_y}(\mathbf{q})$

B

$\mathrm{Re}\tilde{O}_x(\mathbf{q}) + \mathrm{Re}\tilde{O}_y(\mathbf{q})$

$\mathrm{Re}\tilde{O}_x(\mathbf{q}) - \mathrm{Re}\tilde{O}_y(\mathbf{q})$

(1,0)

Q

q_y **-Q** q_x

C

q_y q_x

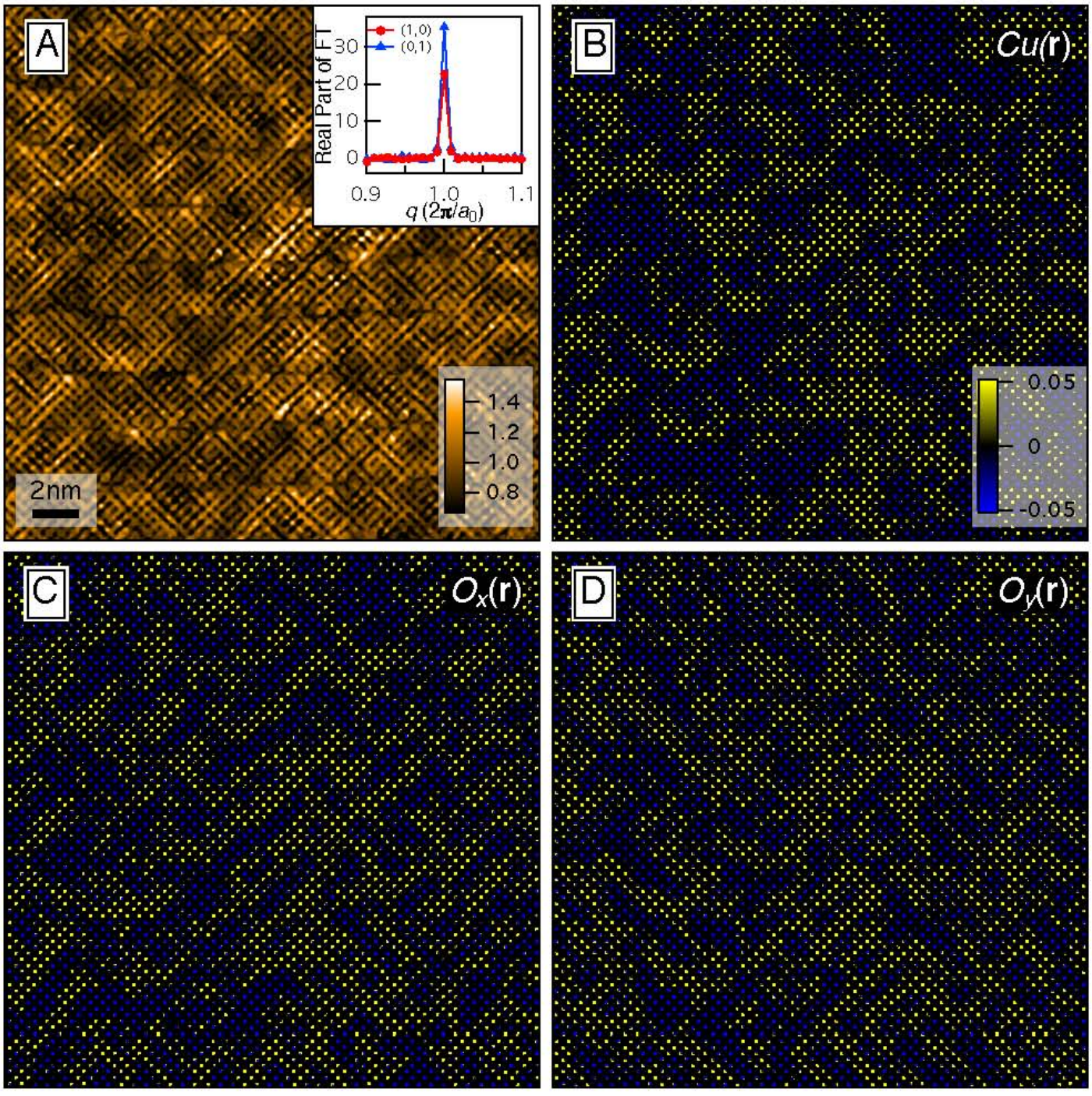
A
Real Part of FT
30
20
10
0
(1,0)
(0,1)
0.9
1.0
1.1
q (2π/a0)
1.4
1.2
1.0
0.8
2nm
B
Cu(r)
0.05
0
-0.05
C
Ox(r)
D
Oy(r)

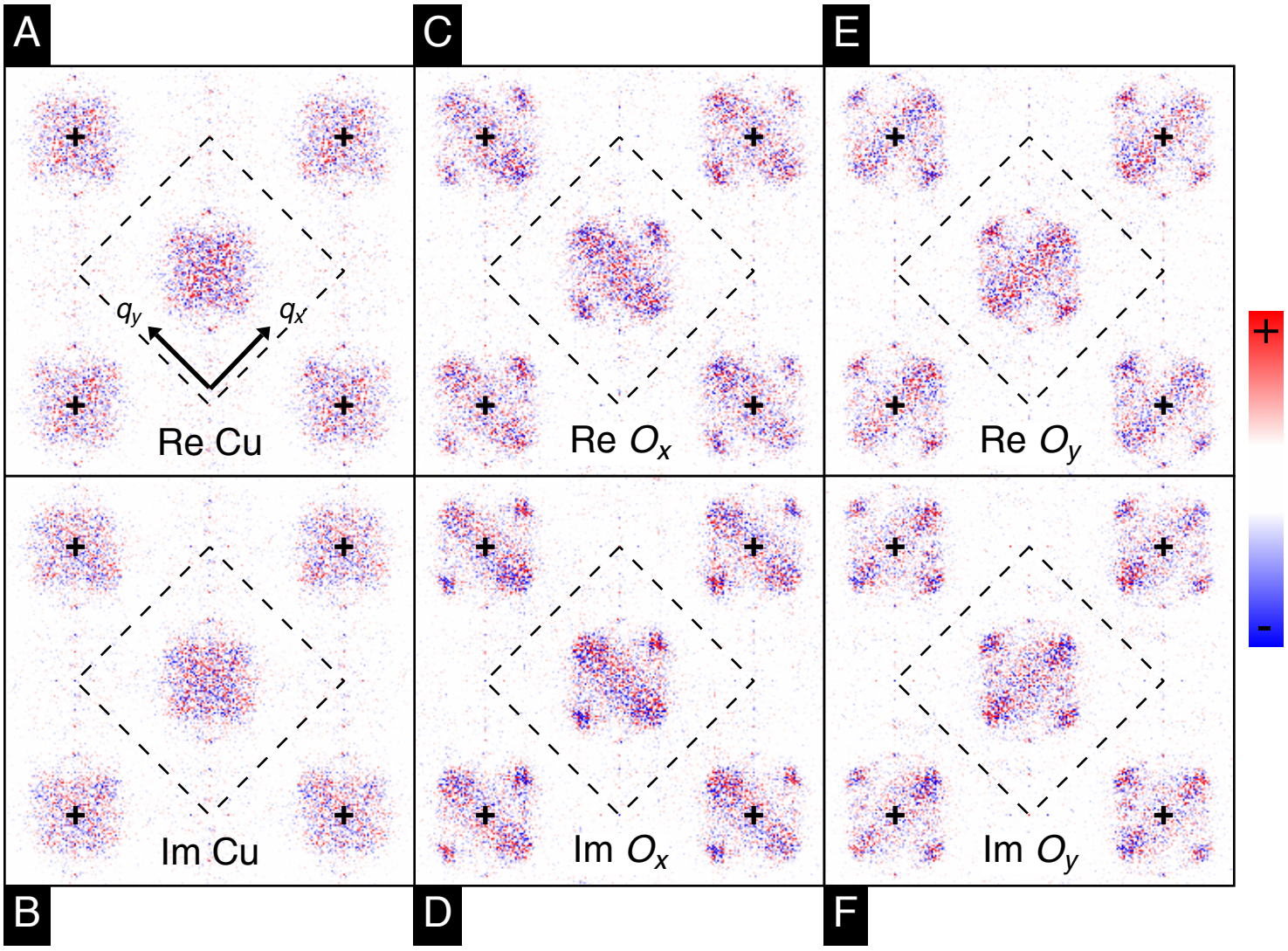
A
C
E
q_y
q_x
Re Cu
Re O_x
Re O_y
Im Cu
Im O_x
Im O_y
+
-
B
D
F

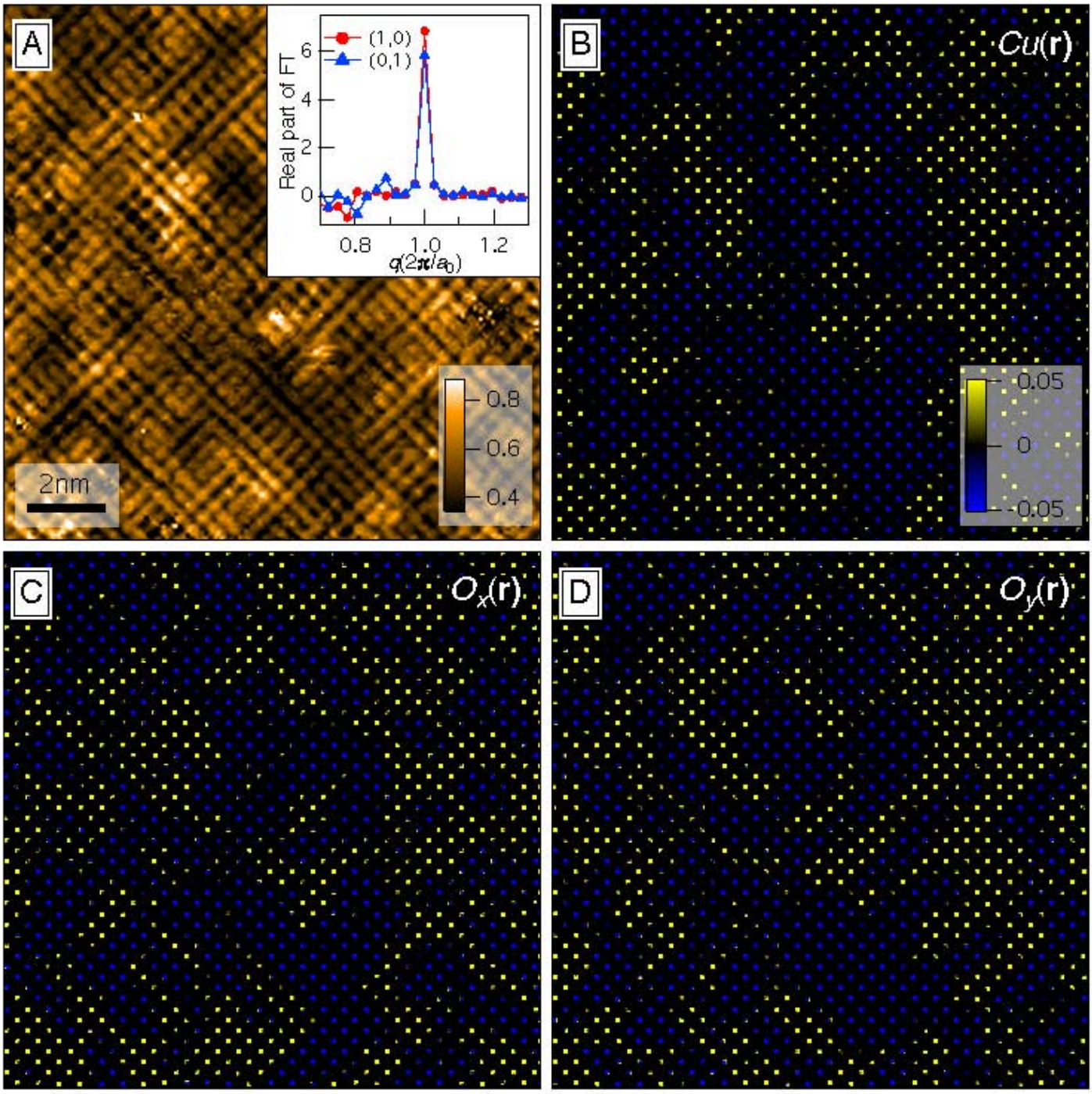
A
Real part of FT
(1,0)
(0,1)
6
4
2
0
0.8
1.0
1.2
q(2π/a0)
0.8
0.6
0.4
2nm
B
Cu(r)
0.05
0
-0.05
C
Ox(r)
D
Oy(r)

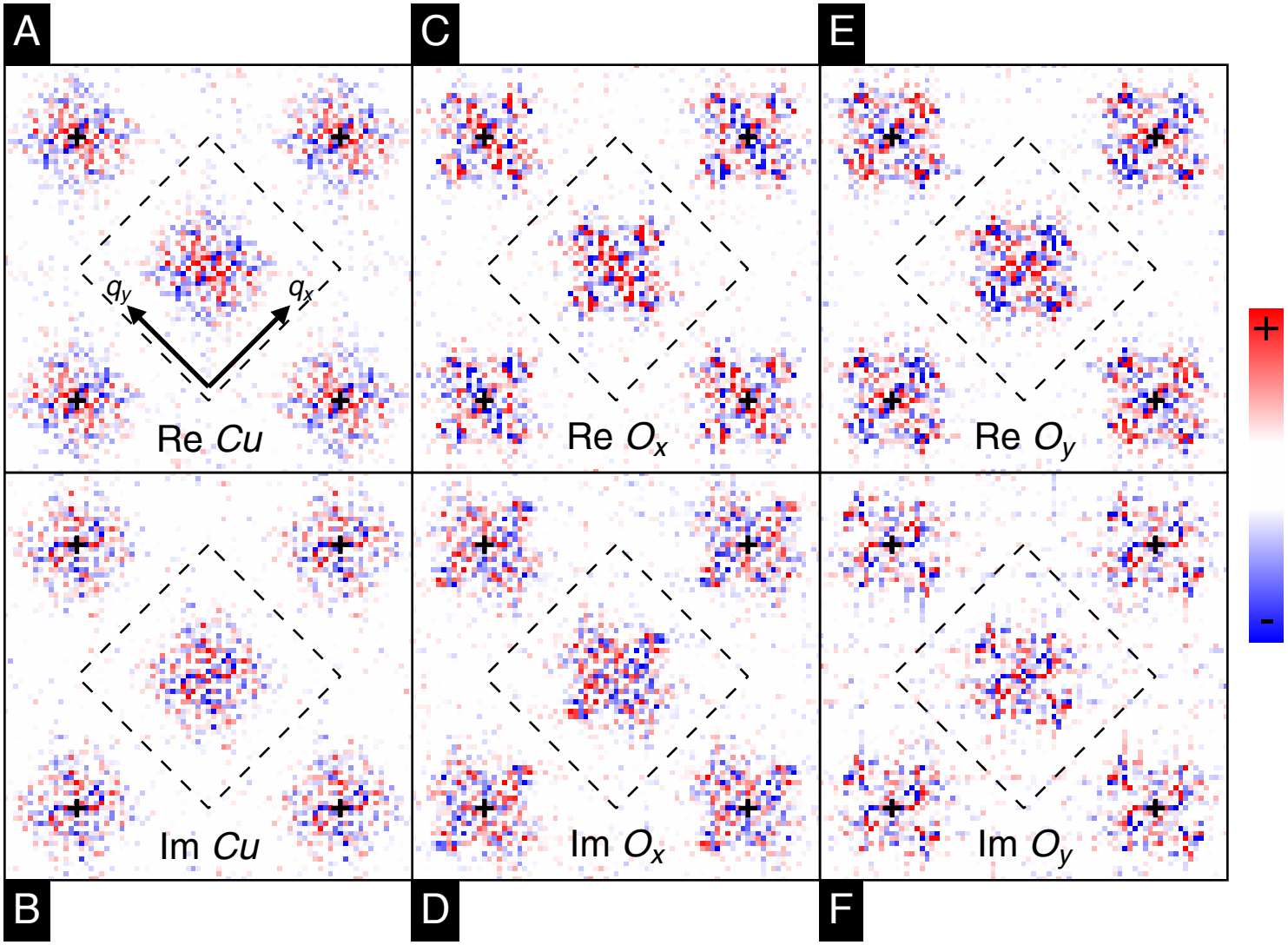
A
C
E
q_y
q_x
Re *Cu*
Re O_x
Re O_y
Im *Cu*
Im O_x
Im O_y
B
D
F
+
-

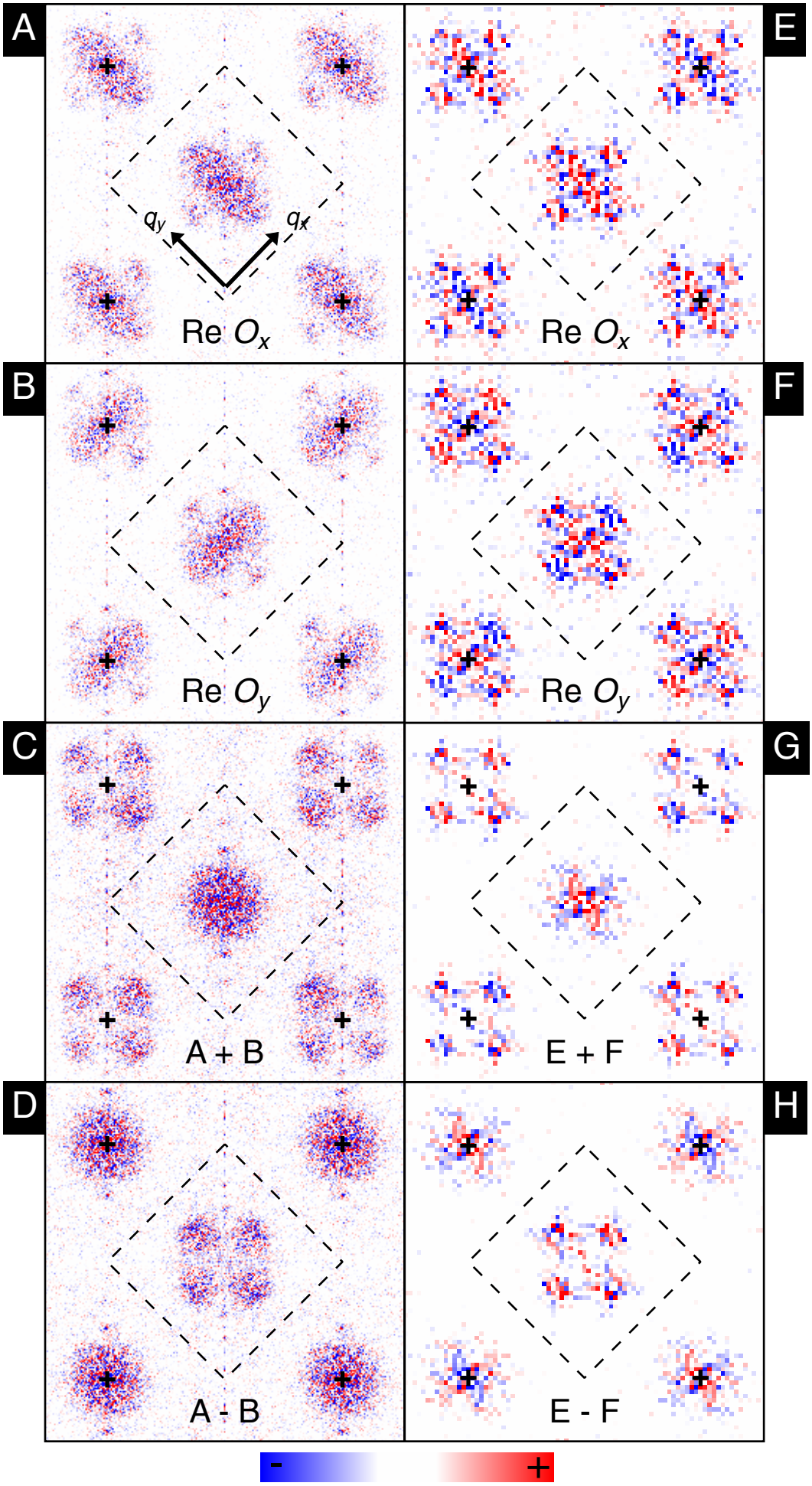
A
E
q_y
q_x
Re O_x
Re O_x
B
F
Re O_y
Re O_y
C
G
A + B
E + F
D
H
A - B
E - F
-
+